2018-06-01

In Situ Analysis of Void Formation at the Flow Front in RTM

Perry August Burton
Brigham Young University

In Situ Analysis of Void Formation at the Flow Front During RTM

Perry August Burton

A thesis submitted to the faculty of
Brigham Young University
in partial fulfillment of the requirements for the degree of

Master of Science

Andrew R. George, Chair
David T. Fullwood
Michael P. Miles

School of Technology

Brigham Young University

ABSTRACT

In Situ Analysis of Void Formation at
the Flow Front During RTM

Perry August Burton
School of Technology, BYU
Master of Science

The purpose of this research is to empirically investigate flow front void formation rates and post-formation bubble mobility behavior for composites produced via resin transfer molding (RTM).

For this study, *in situ* observation of bubble formation and migration was accomplished by photographing resin flow progression during infusion tests of carbon reinforcements. An analysis strategy for use in batch processing sequential image sets is presented. The use of MATLAB to process and analyze binary images of infusions for void content has garnered satisfactory results and has shown that analysis of progressive image sequences can greatly enrich the volume of *in situ* measurements for a given study without compromising the data quality.

Semi-automated MATLAB software analysis employed the representative image area (RIA) method to evaluate v_0. It was found that the shorter the RIA length, and the more it follows the true flow front shape, the more representative the measured v_0 was of the void formation at the flow front.

Experimental evidence of *in situ* bubble formation and mobility behavior is presented. Stitch architecture of NCF reinforcements is shown to influence bubble formation at the flow front. Bubble mobility mechanisms (such as escape and entrapment) are related to stitch orientation relative to the fluid flow direction. Different stitching orientations exhibited different effects on post-formation mobility.

Void formation is presented as a function of flow front velocity. Despite differences in preform configurations (stitch orientation with respect to flow) and injection flowrates, bubbles seem to form in a similar fashion for the 3 infusions of carbon fiber NCF reinforcement analyzed in this study. It is observed that bubbles form at stitch lines, regardless of stitch orientation.

Bubble migration is documented for infusion of NCF reinforcement with stitching at different orientations. Qualitative observations of bubble migration during infusions of a dense preform of STW, plain weave fabric are discussed. Recommendations are given for future studies involving image-based analysis of *in situ* bubble formation and migration.

Keywords: liquid composite molding, voids, bubble flow, fluorescence, *in situ* photography

ACKNOWLEDGEMENTS

I offer my sincere thanks to the faculty of Brigham Young University for the countless lessons and immeasurable impact they have effectuated in my life. My deepest gratitude to my graduate committee for the encouragements and corrections they offered to me throughout the course of this research. I especially thank my graduate committee chair Andrew George. His guidance and infectious enthusiasm have enriched my educational and professional trajectories, something for which I will always be grateful.

I thank the Swedish Institute of Composites (SICOMP) for allowing use of their equipment and facility for the work of this research. It is an honor to have worked in a laboratory with such a pedigree in composites research.

My appreciation goes out to the Society for the Advancement of Material and Process Engineering (SAMPE) Salt Lake City chapter for their dedication to the composites industry and inspiring students to get involved in the world of composites.

I acknowledge and thank my fellow BYU graduate students whose previous work proceeded this research, namely: Mark Brandley, Dave Hoagland, Brock Zobell, Caleb Lystrup, and Kimberly Stevens. My thanks to Cole Childs for his assistance in the present work. To the numerous students who I have had the honor of working with in the BYU Plastics and Composites Lab: I am grateful for all that you have taught me.

Most of all, my heartfelt appreciation and thanks to my wife, Mindy. Her support and sacrifice throughout the course of this work has been incalculable, for which I am forever grateful. I also thank my parents Gideon and Karen for their example and encouragement.

TABLE OF CONTENTS

LIST OF TABLES

LIST OF FIGURES

1 INTRODUCTION

By its very definition, a composite is made up of multiple materials. In engineering the term usually refers to fibers within a polymer matrix. Fibers typically act as the main structural reinforcement, and their relative orientation within the composite is a principle design element. The polymer matrix imparts stiffness and shape to the composite part, aids in transferring loads to the fiber, and can be tailored to address specific characteristics such as toughness and chemical resistance. Composites are stiff, strong, and lightweight - an ideal material for making high-end performance parts (such as aircraft components) which benefit from weight savings.

Applications of composite materials in an increasing number of industries has brought a demand for manufacturing processes capable of producing quality parts at higher volumes. Understanding manufacturing process characteristics drives efforts to reduce cycle times, production costs, and process-induced defects. One example of the latter is the common challenge of voids in producing composite parts, which are air bubbles trapped in the matrix during the manufacturing process. Voids are often formed when resin is first being introduced to the reinforcement fibers. The polymer resin begins as a liquid, is mixed with the fibers, and then solidifies via chemical reaction (in the case of thermosets) or cooling (in the case of thermoplastics). This polymer matrix encapsulates the fibers—as well as any air bubbles present—resulting in the newly-formed polymer/fiber composite. Bubbles trapped within the cured plastic reduce the overall strength of the composite part, and often lead to premature

material failure. Thus, minimizing the formation of voids is a main concern in composites manufacturing.

Autoclave processes have historically been the standard in the manufacture of high performance composites. Low void contents are achievable with autoclaves due to the high pressures involved, but disadvantages include: limitations on allowable part size, slow cycle times, and high costs associated with relevant equipment and materials (such as prepregs).

Liquid Composite Molding (LCM) processes such as Resin Transfer Molding (RTM) have shown potential for producing composite parts with quality comparable to autoclave equivalents, while allowing for much shorter cycle times and lower costs. LCM processes typically consist of infiltrating a dry fibrous reinforcement preform with resin. By using dry fibers instead of prepreg materials manufacturers gain more flexibility with their process and materials, and can eliminate costs such as cold storage (necessary for prepregs). But such added material flexibility comes with a potential increase in process-related defects, like voids (air bubbles). Air bubbles which become trapped within the fiber preform during the molding process become part of the laminate and act to reduce the mechanical properties of the cured composite. As little as 1% volume of voids can compromise part strength by up to 30% (Judd, 1978). Thus, understanding void formation which occurs during composite part manufacture is key for LCM to compete with autoclave processes.

To optimize process parameters to reduce void content requires an understanding of how these voids both form and move during resin impregnation of the fiber reinforcement. Recent studies have related the flow velocity during LCM processing to the void formation rate (Leclerc, 2008; Ruiz, 2006). Understanding how resin flow rate affects final void content is critical to further development of predictive models for LCM processes such as RTM.

For liquid composite molding (LCM) the problem is that predictive models for void formation are currently limited in accuracy or practical applicability. It is not uncommon for a model to yield low fidelity predictions (Arcila 2016), which could stem from oversimplification or generalization of model variables (Liu, 2016; Summerscales, 2017). This is sometimes highlighted when a predictive model is applied to a configuration different to that in which it was developed. The level of detail to which each process variable is considered (for modeling) or evaluated (for experimental evidence) can greatly-affect the discrepancy of simulated versus actual results. Adequate consideration of complex variable interactions (such as: the effect of specific reinforcement configurations on flow front behaviors, the influence of resin injection rates on void formation, factors affecting 3D permeabilities, etc.) has been noted as a key aspect of future modeling development (Celle, 2008; Liu, 2016). Empirical investigation to experimentally uncover, validate, and characterize variables relevant to predicting process-induced voids in LCM will greatly contribute to such efforts.

Understanding void formation is one of the issues that contributes to this complex, "multi-disciplinary nature" of composites (Brandley, 2015). The nature of such manufacturing process problems is that to attempt to isolate a single variable quickly reveals larger, multi-faceted interdependencies. While there have been several recent papers discussing theoretical models to predict void formation and bubble mobility, little literature exists on empirical, *in situ* analysis of void formation rate(s) during liquid composite molding processes.

The purpose of this research is to empirically investigate flow front void formation rates and post-formation bubble mobility behavior for composites produced via resin transfer molding (RTM). Key to this will be gathering data which show void formation as a function of resin flow rate (or at least that some correlation is feasible and warrants further study). Investigating this

relationship across the entire duration of an infusion by collecting multiple *in situ* datapoints is of particular interest, as there has been very little such empirical exploration in the literature. As such, a secondary purpose of this research is to present a strategy for semi-automated *in situ* measurement tools for application in flow visualization studies. Analyzing larger data volumes with such methods can help those working to refine predictive models for simulation applications. For the purpose of supporting such future modeling developments, this research will also include efforts to characterize *in situ* the influence of textile geometry (fabric architecture, orientation) on the void formation and post-formation bubble mobility during RTM. Ultimately the motivation for empirical investigations is to contribute to ongoing developments in higher-fidelity modeling and simulation capabilities, as these will enable manufacturers to better-design and better-control LCM processes for the production of high quality composite laminates.

2 LITERATURE REVIEW

Voids negatively affect the mechanical properties of composite laminates, a concept that is well-documented in the literature (Judd, 1978; Tang, 1987; Almeida, 1994; Olivier, 1995; Wisnom, 1996; Huang, 2005; Guo, 2009; Varna, 1995; Lebel, 2008; Lambert, 2012; Sisodia, 2015). Thus, a main goal of industry's simulation developments is to be able to closely-predict the final void content of a cured part manufactured. The majority of void characterization data already existing in the literature deals with autoclave-cured prepreg materials (Judd, 1978; Tang, 1987; Almeida, 1994; Olivier, 1995; Huang, 2005; Guo, 2009). Such studies traditionally quantify voids with an average void volume fraction throughout the entire laminate-part. This is due to the normally homogeneous void concentration caused by the autoclave oven, where the pressure applied is equal across the laminate surface. Unlike prepreg processing, the void concentration is not homogeneous for a part produced by LCM due to the pressure gradient through the part, which is required for infusion. Due to the complex fiber architecture usually involved in LCM, bubble formation mechanisms are complex, resulting in a variety of bubble sizes and shapes (Hamidi, 2005; Sisodia, 2016). This implies the need for local characterization of voids in a part manufactured by LCM, as opposed to the global average numbers often seen for autoclave-cured prepreg.

2.1 Void Formation

A composite part made via LCM commonly has more voids than a prepreg-produced part, due to the bubble formation which occurs during infusion in LCM (Patel, 1995; Park, 2011; Hamidi, 2004). This occurs due to a phenomenon termed mechanical entrapment of bubbles. Previous literature has divided such bubble entrapment according to the dual-scale nature of the flow through a typical composite reinforcement material, i.e. consisting of bundles (e.g. "tow" for carbon, as is the case in this study) of individual filaments. Flow of fluid between the individual filaments (intra-tow) is induced by capillary force, whereas flow between tows (inter-tow) is dictated by viscous force (Ravey, 2014). According to Breard, three stages of resin flow occur: (i) filling of inter-tow space, (ii) filling of intra-tow spaces, and (iii) two-phase flow, which occurs after maximum possible saturation has occurred (Breard, 2003).

Permeability (K) is a property of reinforcement material (Breard, 2003), with dual-scale fabric exhibiting different permeability for bulk and tow saturations (Kuentzer, 2006). As described by Endruweit (Endruweit, 2011), composite permeability (and the associated flow) can be considered at three general scales**:**

- Macro-scale (~m), as dictated by general geometric features of the part.
- Meso-scale (~mm), which includes inter-tow area between fiber bundles.
- Micro-scale (~μm), intra-tow areas within fiber bundles, area between individual fiber filaments.

Simulation predictions of mold filling are dependent on correct permeability being known (Breard, 2003).

Void formation models are usually meant to predict the voids created at the flow front for a particular instantaneous bulk (inter-tow) flow front velocity (v) at that point in time and space.

Void content is often represented by the term v_0 in the literature, and is considered as such in the present work. Capillary flow is a function of reinforcement architecture and not sensitive to the LCM applied pressure, thus capillary flow rates are more or less constant during infusion. As the bulk flow rate usually varies, and in any case never the exact same rate as the capillary flow, the flow rate is faster either in the tow or in between the tows. Smaller "micro-void" bubbles are formed inside the tow and larger "macro-void" bubbles are formed in the fluid-filled inter-tow gaps. Higher applied pressures cause a higher bulk flow velocity resulting in faster flow in between the tows, outpacing the capillary flow into the tows, thus trapping intra-tow bubbles (Rohatgi, 1996). Lower applied pressures cause the opposite case, where capillary flow outpaces the inter-tow flow, trapping larger inter-tow bubbles (Patel, 1995; Matsuzaki, 2014).

There is substantial treatment given in the literature regarding the topic of optimum infiltration velocity, a rate for which the overall void formation is minimized by balancing the macro- and micro-scale flow during the infusion phase of LCM (Patel, 1995; Ruiz, 2005; Lundstrom, 2000; Causse, 2018). The overall concept of macro- and micro-void formation as a function of resin velocity is commonly presented as a simplified illustration, an example of which is shown in Figure 2-1. The curve shown in the figure below represents the anticipated void content (v_0) for a given injection velocity (v), though there is no definite agreement within the literature as to the shape of such a curve. Much data and discussion has been previously presented in an effort to support the concept of this $v_0(v)$ function (Patel, 1996; Leclerc, 2008; Park, 2011), though there has yet to be a general consensus on the specific curve shape that is expected. Some present the curve as more of a sharp "V" shape, with strictly linear parts which sharply intersect at the predicted "optimal" velocity value or value range (Gourichon 2006;

Leclerc, 2008; Ruiz, 2006). As shown in Figure 2-1 (Causse, 2018), more-recent illustrations present a curved transition between the pre- and post-optimal velocities.

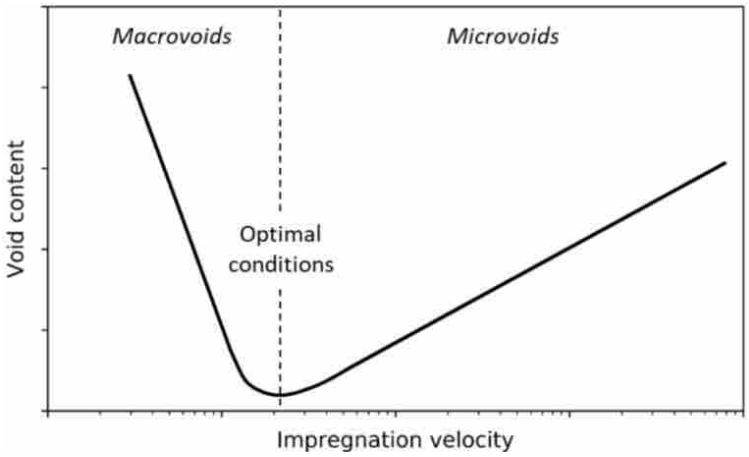

Figure 2-1: Conceptual Illustration of Void Content as a Function of Resin Velocity

Note that the capillary number (or a version thereof) is sometimes considered instead of resin velocity in such discussions. Since the capillary number simply includes consideration for resin characteristics in addition to injection velocity, such as viscosity and surface tension, for the purposes of the present explanation it may be roughly considered as conceptually equivalent to velocity.

It has been argued that for LCM processing more importance should be placed on addressing formation of macro-voids due to their higher contribution to overall void volume fraction (compared to micro-voids) (Leclerc, 2008) and to part mechanical properties (Sisodia, 2015; Lambert, 2012).

2.2 Measurement Methods for Voids

Although the concept of an optimum flow velocity for minimal void formation is of great value to the composites industry, in practice this idea has been slow in its application, mainly due to the difficulty of characterizing that optimal flow velocity. This is evidenced by the number of theoretical models presented in the literature based on a fluid dynamics approach to predicting void formation with little experimental validation (Frishfelds, 2008; Lebel, 2014). Acceptable 2D models for simulating resin flow in LCM have been established (Trochu, 2006) but fall short when predicting RTM flow behavior in thicker parts. This is partially due to the additional elements which must be considered when scaling the numerical simulations to close-to-real-world material scenarios, often involving more complex experimental characterization.

2.2.1 *Ex Situ* Void Characterization

Void characterization is most often done *ex situ* after a laminate has been cured. This allows the most flexibility with test methods given a solid cured part. For cured composite laminates, various measurement methods are available to evaluate characteristics such as material volume fractions, quantity and location of porosity, laminate damage, and so on. Most are suitable for use as stand-alone techniques, though it is common for more than one method to be employed when there are multiple characteristics of interest to be measured.

Microscopy is an established method which offers the benefit of visually characterizing void location and morphology (Leclerc, 2008). Variants common to the composites industry include optical microscopy and scanning electron microscope (Ray, 2007). An advantage of microscopy is that attributes of individual voids (those which can be seen in the sample's cross section) can be evaluated and compared (Little, 2012). Careful sample preparation is critical.

Cross section surfaces must be polished and cleaned (Cann, 2008). Images taken via microscope are then digitally processed and analyzed for void content.

When investigating void content of cured laminates, it is typical for samples to be taken with the cross-section perpendicular to principal fiber direction. Thus, for composite laminates with many fiber ply orientations multiple samples must be cross sectioned to allow inspection of fibers in all directions of interest (Hurtado, 2015). Images are analyzed using either the fiber counting method (which counts individual fibers, seen as distinct areas within the image) or the areal method (assumes volume fractions based on areas of image that are the color of fiber or voids) (Cann, 2008). Both such methods typically employ software tools as means of evaluating image contents, with user-set thresholds (such as pixel contrast) denoting what differentiates the areas of interest in a photo. This analysis is limited to 2D images which results in only a partial picture of void characterization (i.e. detection of a specific void cannot yield any information beyond its size and location within the observed laminate cross section). Preparation is particularly difficult for composite samples due to the potential for frayed fibers to come loose and damage the surface finish during polishing (Little, 2012).

An ASTM standard exists for measurement of constituent contents of a composite material, namely, the fiber, matrix, and void volumetric percentages (ASTM D3171-2015). This test method covers both matrix digestion and combustion methods. For the method of matrix digestion, a composite sample of known density first undergoes submersion in hot acid (to dissolve matrix material). The remaining fiber content is then washed and weighed post-digestion. Used on its own this method can be useful for determination of fiber volume fraction, but often includes the assumption that void content is negligible (Carlsson, 2014).

Like digestion, the combustion method determines a composite sample's volume fraction(s) by removal of matrix material. Heating the sample to elevated temperatures (typically in an oven) achieves resin burn-off and allows the remaining fiber content to be evaluated. Combustion is sometimes chosen over digestion to evaluate glass fiber composites (Carlsson, 2014).

Ultrasonic non-destructive inspection (NDI) methods (such as C-scan) are especially useful when the goal is to characterize void content beyond simple volume fraction estimates. Measurements are taken by scanning the composite material and observing signal attenuation, which can be affected by voids, resin cure, dry spots, laminate damage, and fiber (Stone, 1975). Since there will always be some measure of signal degradation as waves pass through the composite, threshold values on permissible signal loss are set to delineate what constitutes a defect. It is common for software to be employed to scan and interpret received signal data according to the threshold parameters set by the user (Kas, 2005), which can help avoid subjective evaluation of scan results. An absorption coefficient is found as a function of the average attenuation level. Correlating void quantity with ultrasonic attenuation can be done by determining void volume fraction via digestion (or combustion). Void content can then be shown as a function of the absorption coefficient (de Almeida, 1994; Liu, 2006). Recent studies have investigated ultrasound as a possible means of gathering real-time, *in situ* resin flow data in LCM production processes (Liu, 2014). Measurement data gathered via ultrasound are inherently 2-dimensional, which partially-limits the level of characterization possible for a given measurable (Kas, 2005).

X-ray inspection (micro-CT) is a less-common void measurement method. X-ray offers accurate, 3D analysis of void contents, but involves expensive equipment, and is currently limited to inspecting small samples per lengthy scan times (Little, 2012).

2.2.2 *In Situ* Void Characterization

Ex situ void characterization is not applicable to void formation studies, as the formed bubbles continue to move and change shape after their formation up until the gelation and subsequent cure of the matrix. Thus, recent studies have presented methodologies to characterize the bubbles *in situ* during infusion. This becomes inherently more difficult as the material is enclosed behind thick tooling, no cross-sectional optical analysis is allowable due to the still-liquid matrix, and the fact that most imaging techniques such as ultrasound and X-ray are tailored for solid materials.

Some methodologies presented in the literature forego imaging the bubbles themselves, electing to instead simply measure the air volume present in the material by changes in either electrical conductivity (Gueroult, 2014), thermal conductivity (Villiere, 2015), ultrasound attenuation (Saraswat, 2007), flowrate (difference between inlet and vent) (Gourichon, 2006), or light transmission (Lebel, 2017). All but the latter are applicable to both carbon and fiberglass reinforcements. The opacity of carbon fibers (compared to translucent glass) hinders any light transmission studies of saturation or voids in composite reinforcements.

The above mentioned *in situ* methods do not give any idea of bubble size, shape or velocity, which would all be useful for predictive models on bubble formation, mobility and their effect on mechanical properties. Light-based photography has been used for void characterization in fiberglass reinforcements (Patel, 1995; Seto, 2011; Lebel, 2014). But no such study showing *in situ* bubble morphology has been seen in the literature for carbon

reinforcements, due to the already-mentioned challenge of the opacity of the fibers. This is a significant problem to such research, as void studies are usually only a concern for the high-performance composites industry, which uses carbon fiber more often than glass fiber due to the higher mechanical properties and lower density.

High resolution synchrotron computed tomography (SRCT), a form of x-ray imaging, has been used to generate volumetric images of void formation in a single glass roving (Vila, 2015), and could theoretically be done with carbon as well. But the limitations on sample size for such testing prevent characterization of a larger fabric sample.

Thus, a critical need in LCM process optimization is a method to characterize bubbles *in situ* in a carbon reinforcement.

2.3 Void Mobility Modeling

Void formation models in the literature tend to ignore post-formation bubble migration, greatly-reducing their practical applicability to RTM processes where flow rates are high (and thus void migration more apparent). Many of these formed bubbles, especially the smaller intra-tow bubbles, remain trapped where they were formed as the highly compact reinforcement architecture hinders movement in the flow direction (Lundstrom, 1994; Gourichon, 2006). Bubbles eventually diffuse into solution (Henry's Law) as the local fluid pressure continues to increase due to the flow front continuing to advance farther from a bubble's location (Lundstrom, 1997). Some bubbles, especially the ones located in the inter-tow channels where flow is easier, manage to escape from their place of formation, and are transported quickly toward the flow front by the pressure gradient (Frishfelds, 2008). Such bubble mobility depends on the inter-bundle gap width, the applied pressure, and the bubble size. As the resin pressure continues to increase at a given location during the filling time in LCM, the bubbles decrease in

size by both the Ideal Gas Law and dissolution (Henry's Law) until the bubble is small enough to escape (Lundstrom, 1997; Shih, 2002; Kang, 2004). This pressure gradient causes a higher void content to be observed by the inlet than by the flow front (Lundstrom, 1994). Some mobile bubbles reach the flow front and escape to the air on the downstream side of the front.

Models for void mobility must be able to combine with formation models to yield "end result" simulations that are representative of real-world outcomes. Anisotropic nature of woven fabrics, fiber orientation direction, and processing parameters (such as resin velocity) all affect void formation, flow, and distribution (Matuzaki, 2015; Frishfelds, 2008). "Bubble Mobility" is a measure of void velocity with respect to the resin matrix and is considered as resulting from process and material characteristics (Gangloff, 2014). In general, bubble mobility describes whether bubbles will move faster or slower than the surrounding resin flow. Bubble movement models are usually meant to predict the final location and size of a bubble after formation. But again, these models suffer from a lack of experimental data on bubble mobility, especially in carbon reinforcements.

3 METHODOLOGY

3.1 Constant Velocity vs. Constant Flowrate Experimentation

Previous work with this fluorescent in situ void measurement method was done with a constant pressure based infusion (Lystrup, 2018; Zobell, 2017). Such an infusion entails a non-linear decrease in the flow front velocity (v) during a uni-directional flow test. The reduction in velocity is due to distributing the same available pressure gradient across a longer filled regime (L). The velocity is proportional to the pressure gradient (dP/dx) at the flow front ($x=L$). The pressures at the inlet and flow front remain the same, but as the flow front moves toward the vent the pressure differential gets spread across a longer filled sample, thus reducing the pressure gradient. An alternative explanation is that the sample itself behaves like a lattice of many small pipes: as the front moves away from the pressure source the applied pressure at the flow front decreases due to increasing shear from the many small pipes.

This complex velocity history complicates a statistical study of the relationship between void formation and flow front velocity. For constant-pressure injections, any measurement of void content near the flow front is made at a velocity that cannot be repeated during that same experiment. Thus it was thought that a constant flowrate (Q) experiment, where an infusion could be made at a single flow velocity, might be better suited to this study. This would allow an evaluation of the repeatability of void formation during an entire test, and then repeat the infusion at another flow rate.

A constant flowrate experiment requires more specialized equipment than a constant pressure test. The latter only requires a pressurized air source and a pressure pot with an air flow valve and a pressure gauge. The former usually employs a piston and cylinder setup, where the test fluid is held in the cylinder, and forced out into the mold by the piston moving at a carefully controlled constant displacement rate. This type of "injection machine" forces the infusion to occur at a constant flowrate Q and, as the sample cross-section A and porosity (φ) are constant in the mold, v is then also held constant throughout the infusion. The usual limitation to this type of constancy is the maximum pressure capabilities of the injection machine, the connecting tubing to the tool and the tool itself; the applied pressure on the piston to maintain a velocity rises proportional to the increasing length L. It is therefore common with the typical permeability test sample lengths (i.e. 200 to 500 mm) to reach a maximum pressure limit before finishing the infusion, at which point the infusion then proceeds as a constant pressure infusion (with continued movement of the piston, limited by the prescribed maximum pressure threshold).

Equipment expense is another limitation of constant Q testing. An injection machine with capabilities to control the piston displacement rate can range in cost from $50,000 to $150,000 depending on the maximum sustainable pressure, fluid volume capacity, and resolution in displacement control. Inquiries were made to a wide range of academic and industry contacts about the possibility of borrowing or using such a machine for this study. Of those contacted, the Swedish Institute of Composites (SICOMP) was the only laboratory properly equipped and willing to allow use of their working injection machine. Thus the tooling, fabric samples, and photography equipment were transported to the lab (located in Piteå, Sweden) for the experimentation.

3.2 Equipment and Tooling

Mold tooling primarily consisted of a unidirectional permeability test bench (see Figure 3-1, adapted from Hoagland, 2017). This tool has been used for permeability benchmark studies and is described elsewhere (Hoagland, 2017). The tool consists of a steel plate base (4340 steel), trued flat on a surface grinder, with threaded holes for inlet and vent port fittings and through holes for clamp bolts. A 75 mm thick polymethylmethacrylate (PMMA) plate serves for the mold top half. An approximately 15 mm wide removable silicone gasket defines and seals the dimensions of the mold cavity area. Six large (Grade 8) bolts torqued to at least 20 ft·lbs hold the mold together, passing through the steel base, PMMA top, and C-channel profiles laid along the long edges of the mold to distribute the applied bolt pressure. The thickness in the mold cavity was set by shimming with steel thickness gauge strips to a 1.3 mm gap height for all tests.

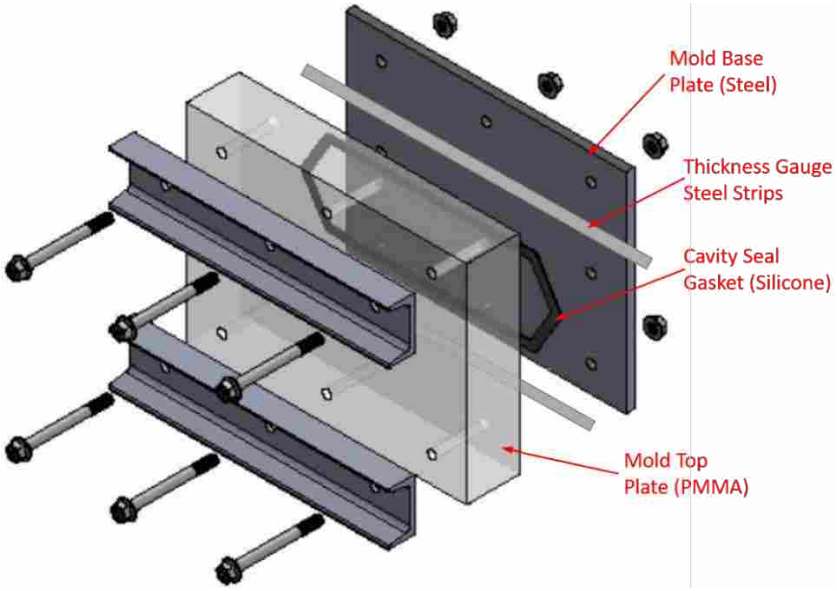

Figure 3-1: Exploded Assembly View of the Mold Tooling

The injection machine used is an ISOJET system (ISOJET Equipements, France). The test fluid was added to the cylinder in a large batch, and a typical infusion plastic flexible pipe was used to connect the cylinder outlet to the mold inlet. No heating was done during any of the infusions; the test fluid remained at room temperature. For each of the infusions the injection machine was set to a constant flowrate. During injection the machine constantly samples and logs the injected volume (as calculated via cylinder piston displacement) and the applied pressure required to maintain the specified flowrate.

In addition to the injection machine's onboard sensor, a dedicated, high-resolution pressure sensor was incorporated into the experimental setup. This was done to have a secondary measurement of the applied pressure on the fluid as it entered the mold, and was accomplished by attaching the sensor to the inlet line via a T-joint placed just before the mold inlet fitting.

3.3 Test Fluid

The test fluid consisted of rapeseed (canola) oil with a UV fluorescent tracer dye (Tracer Products TP34000601), which was added to be approximately 5% of the solution volume. The viscosity (μ) of the mixed oil and dye solution was measured by a rheometer as a function of temperature (T) (the data for which is shown in Figure 3-2), with a room temperature viscosity of approximately 64 mPa·s.

It is unknown as to why the viscosity data from 20°C up to 23.5°C appear to be the same or lower than the readings at 24°C, as viscosity typically exhibits a fairly linear relationship with temperature. The unexpected trend in viscosity was not considered significant to the test results in this study as the ambient temperature was recorded throughout each infusion and was observed to remain fairly constant, typically staying within 1°C of the initial room temperature

noted for the entire duration of each infusion test. Thus it was assumed that the viscosity value for the given start temperature also remained constant for the entire duration of each test infusion.

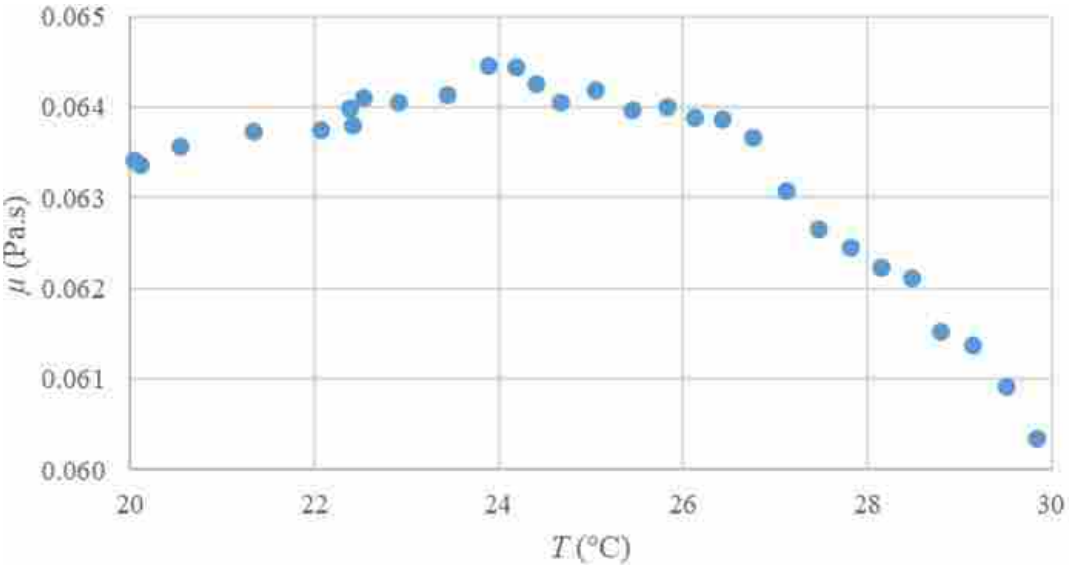

Figure 3-2: Measured Rheometry Data for Oil and Dye Solution

3.4 Reinforcements

The two reinforcements used were chosen as typical carbon fiber fabrics used in the high-performance composites industry. The first was VectorPly C-BX 1800 carbon +45°/-45° biaxial non-crimped-fabric (NCF) with areal weight of 623 g/m^2 and chain stitching along the machine (warp) direction. The second was Oxeon TeXtreme 1003 carbon spread-tow-weave (STW), plain weave, with areal weight of 92 g/m^2 (of which 10 g/m^2 is a polymer binder veil applied by the manufacturer on the fabric surfaces).

3.5 Test Infusions

Table 3-1 illustrates the infusions performed during the visit to SICOMP. The number of ply layers in each sample is recorded there along with the calculated volumetric fiber fraction (v_F). All plies were oriented in the same direction; the orientation listed represents the angle between the machine (warp) direction of the sample plies and the flow direction during the experiment. Note for the NCF material this meant that the only effective difference between 90° and 0° orientation was the direction of the stitching fiber; the principle reinforcement fibers' direction did not change (carbon tows remained oriented at +45°/-45° relative to the direction of flow). The flowrate (Q) value shown is what was programmed on the RTM injection machine for each corresponding infusion.

Table 3-1: Test Plan of Infusions

Test	*Material*	*Plies*	v_F *(%)*	*Orientation*	Q *(cm^3/min)*
T1	NCF	2	54	90°	10
T2	NCF	2	54	90°	12
T3	NCF	2	54	0°	7
T4	STW	14	56	0°	2
T5	STW	14	56	0°	7
T6	STW	14	56	45°	4
T7	STW	14	56	45°	7

The preform sample size was designated as 300 mm x 50 mm. Each ply was cut to size at SICOMP via a CNC ultrasonic cutting table, a tool intended specifically for accurately kit cutting dry reinforcement fabrics, and then assembled into a dry stack preform by hand immediately prior to being placed in the mold cavity. Care was taken to align the ply edges relative to each other so that the overall edge of the fiber stack was as flush as possible when placed onto the steel mold base plate.

The silicone seal gasket was not adhered to either mold half, which allowed for removal and thorough cleaning of both the mold and seal between tests. This also allowed for the seal to be moved into position right up against the long preform edges, thus reducing the propensity for race-tracking by eliminating gaps between the seal and fiber stack.

An adhesive-backed paper strip with graduated measurement markings was placed directly on top of an area of the silicone seal gasket as a calibration standard for image analysis. Placing the ruler directly on the silicone seal effectively ensured it was on the same spatial plane as the voids observed in the test fluid (i.e. against the downward facing side of the acrylic mold half).

3.6 Photography

In situ observation of infusions was accomplished by photographing resin flow progression during the infusion phase of each test. Two DSLR cameras (SONY Alpha SLT-A77V) were held in static position above the mold on a single tripod rail mount (Figure 3-3, adapted from Zobell, 2017). The rail mount, made from 80/20 aluminum extrusion, was purpose-built for this study to facilitate a simple, repeatable way to position cameras for image capture of each test. Both cameras were equipped with the same macro lens (Sigma 50 mm F2.8) and placed at a distance from the mold which allowed for each to capture just over half (approximately 150 mm) of the mold cavity length in their field of view.

Both cameras were connected to the same shutter timer remote control (Pixel TW-283/S1) to allow for synchronized, regular-interval image capture. A wireless remote would activate the shutter timer unit, which would then automatically trigger the cameras to take images at a user-specified time interval value (in seconds). For the data presented in this study the interval time between image capture was 2 seconds.

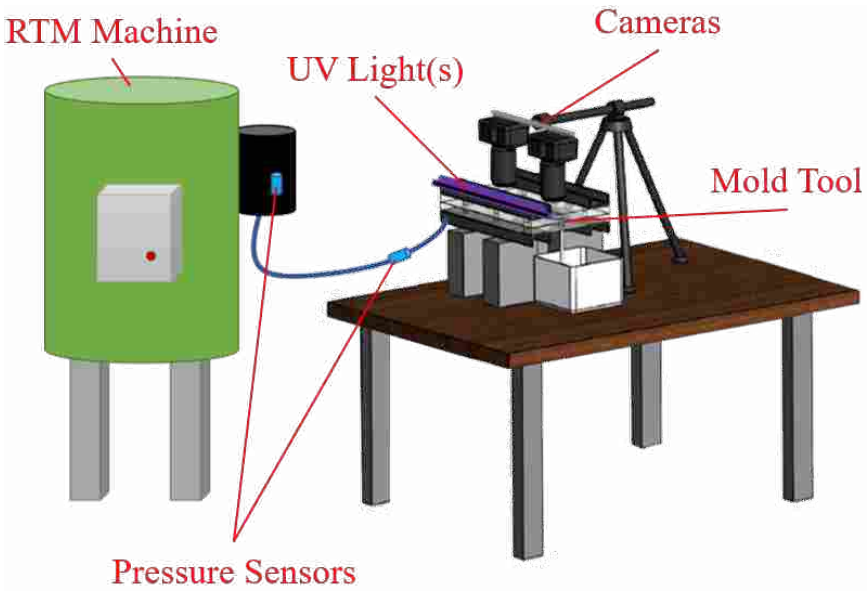

Figure 3-3: Equipment Diagram of Experimental Setup

UV lamps were utilized to highlight the tracer dye in the test fluid and provide excellent bubble-to-fluid contrast during infusions, a method established in previous work (Zobell, 2017). These were positioned either immediately above the acrylic mold top or directly on the steel C-channels, with care taken to place lamps as close to the mold as possible without obstructing camera view of the preform.

During each test a box was placed as a shroud over the entire mold and UV lamp setup to prevent ambient light from reaching the sample. Holes cut in the shroud allowed for the front of the camera lenses to have an unhindered view of the preform. Additional minor holes allowed for the fluid inlet line, power and data chords to run into the shrouded area. To further eliminate any light leakage into the preform area and provide as much control of image exposure as possible, fabric was draped over the entire setup as a second shroud.

Camera settings were chosen to compliment the anticipated test conditions. Both cameras were set to aperture priority shooting mode and were given the same user-specified settings such

as standard (neutral) color mode and no exposure compensation. Though aperture priority mode will automatically adjust shutter speed and ISO settings to achieve optimized photo results, a maximum-allowed ISO value was set to limit the amount of sensor noise recorded in images. Such pixel noise negatively affects software driven image analysis, and thus was considered a key factor in the quality of image data captured.

The cameras were connected to external display screens outside of the shrouded area, which allowed real-time monitoring of infusion progress and key camera aspects (such as quality of image focus, available memory, and battery level) during each test.

3.7 Image Analysis

The general image analysis process followed accepted industry methods for measuring void content captured in a photo: original color images were converted to black and white binary images from which void analysis data could then be obtained. (A more-detailed outline of this workflow is given later in this section.) Such analysis was accomplished via MATLAB code. For the work of this study the strategy and concepts behind the scripts and functions used were developed on the backbone of excellent work by Kimberly Stevens and Caleb Lystrup (Stevens, 2018; Lystrup, 2018). MATLAB was employed to make the image conversion and analysis workflow as objective and accurate as possible. The software was tailored to batch process data from entire image sequences. This was determined to be a key methodology component of the presented flow visualization study as it would show that semi-automated analysis of progressive image sequences can yield a large volume of *in situ* measurement data.

For the purposes of the semi-automated void content measurement, it was assumed that the camera(s) and mold tooling remained statically-positioned during the photography of each

infusion test. In the following discussion an image sequence is a group of specific images which were captured (at progressively-later times) during the same infusion.

Analysis of an infusion first began with specifying an image sequence to represent the general flow progression of the entire test. Images were chosen which showed the flow front position at progressive distances from the fluid inlet (e.g. images that showed the flow front progress at 10 mm, 20 mm, 30 mm, etc., relative to the inlet). Note that during this stage of image selection the flow front position was simply estimated by the user (specific flow front locations would be calculated later on via MATLAB, outlined below). Lists of which specific images to analyze were compiled for T1, T2, and T3. The subsequent processes of binary conversion and data analysis via MATLAB would then reference the image sequence list which corresponded to the infusion being considered for analysis. A detailed workflow for the MATLAB image sequence tools used in this study is given in the following section.

3.7.1 MATLAB Workflow

An initial program defined a few global parameters which would eventually be applied to the entire image sequence. A sample image was selected from the image sequence to represent all the images from that sequence. Image scale was determined by measuring the pixel length of the calibration standard (see Figure 3-4A). An option to specify a correctional image rotation angle was given in case the mold cavity area was not squarely-aligned within the image. It was necessary to ensure the flow direction was shown parallel to the image x-axis (axis along image width), with flow progressing from left to right, as subsequent measurement data was taken with respect to such a global reference frame.

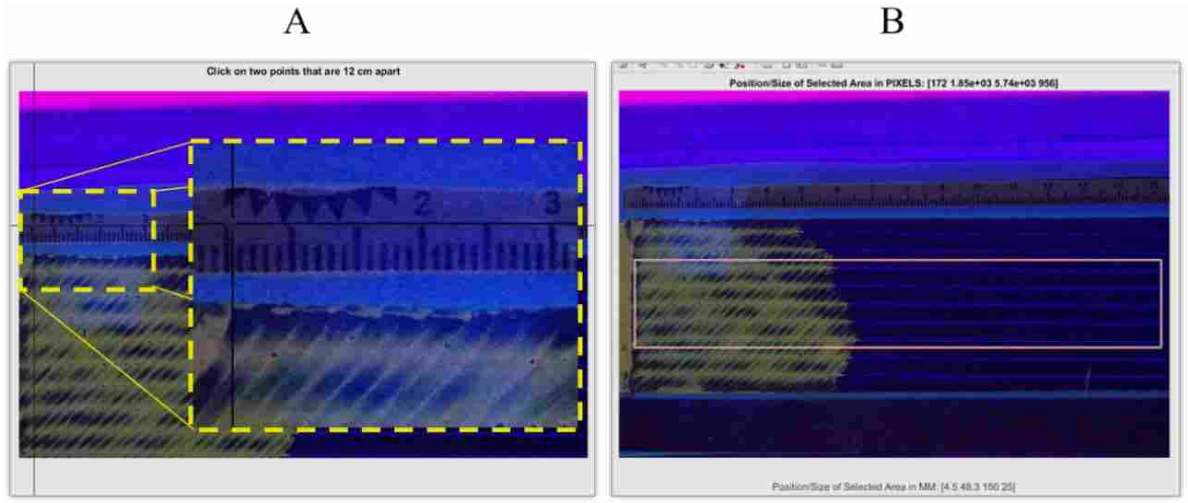

Figure 3-4: Screenshots of Preliminary MATLAB Program

The region of interest within the image bounds (e.g. the preform area to analyze for void content), termed the "representative image area" (RIA) in this paper, was then defined. (The choice of RIA, as well as its further subdivisions, will be discussed later in this paper.) The user would specify the width and length of the intended RIA in millimeters. A bounding box of the specified size would be superimposed onto the sample image. The user could then position the box by dragging it within the sample image (see Figure 3-4B). The area within the box was designated as the area to analyze, all of the image area outside of the box perimeter was ignored. With the size and location of the RIA defined, the pixel address relative to the overall image was recorded. Finally, the values for image scale and RIA pixel address (as well as image rotation angle, if applicable) were output in a MATLAB variables file.

Note that for the remainder of this paper, the term "RIA" will now refer to various image areas that are specified within the initial RIA bounding box first described and shown in Figure 3-4B. Detailed explanation of this is given in the following section (3.7.2).

The majority of software-driven analysis was then accomplished with a second program. To begin, user-specified settings were put into place which were to remain in effect for the analysis of all images in a given batch. These settings were defined with the following process: The list of individual images that made up the given image sequence was specified, and values for image scale and RIA position were loaded via the file output from the initial program. The user was prompted to specify the file folder location of the raw source images, as well as where to save the data and image files output by the program. The various RIA upstream boundary positions were specified in millimeters (a detailed discussion of this is given in the following section). Lastly, the minimum and maximum allowed pixel region sizes, along with an eccentricity limit, were defined for the filtering tools that would be applied to clean up the binary images of voids.

With the settings defined, the program now entered a processing loop. The first part of this loop dealt with converting raw photos to binary images. Figure 3-5 illustrates the general MATLAB image conversion workflow, with Images A through E showing the same image at different stages of the conversion process. The second part of the loop extracted v_0 data from the binary images for the different RIAs. With the image sequence list as a reference, each raw image file was passed through the processing loop and underwent the following:

The raw image was cropped to the pre-defined RIA size. If an image rotation angle had been specified then this was applied to the image before it was cropped. The cropped image was then color segmented into its respective RGB channels, resulting in 3 grayscale images. For

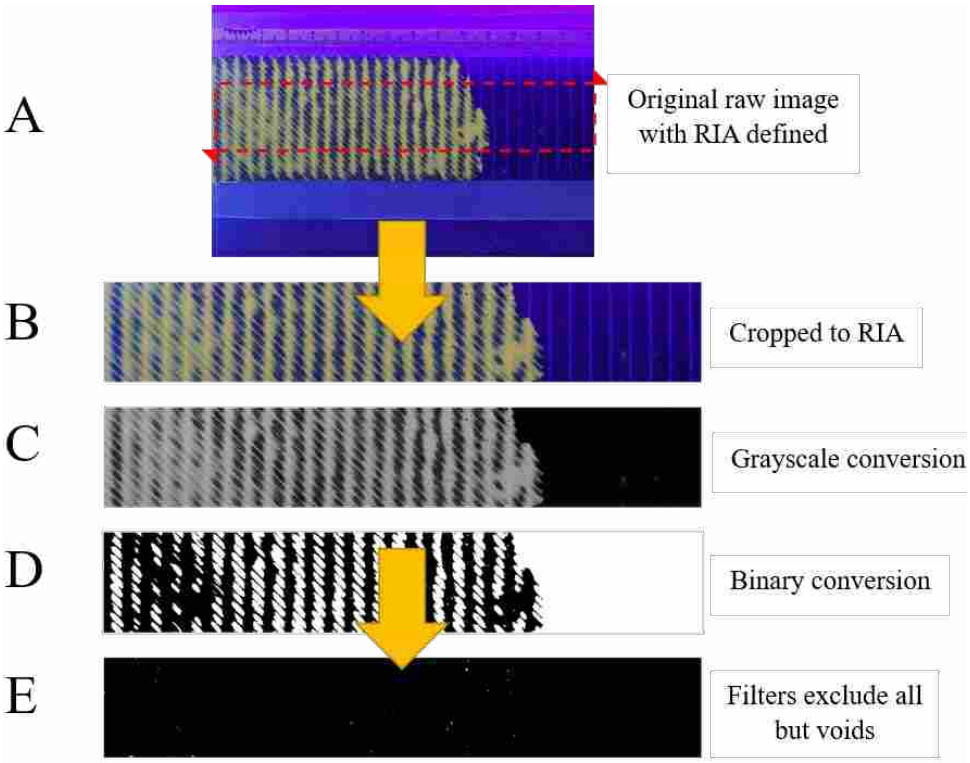

Figure 3-5: Example of the General MATLAB Image Conversion Progression

each grayscale image an ideal threshold value was calculated via Otsu's method (Otsu, 1979), such that the black-to-white variance would be minimized in the resultant binary image. Threshold values were then applied to produce a preliminary binary image from each separate color channel of the source image. These separate binary images were then combined to yield an unfiltered, composite binary image with maximum detail which could be further-refined in subsequent steps. This resultant image was true binary, with each pixel limited strictly to a logical value of either 0 or 1 (represented visually by black and white). An example of a binary image at this stage is illustrated in Figure 3-6A.

A copy of the binary image was passed to a function written by Kimberly Stevens (Stevens, 2018). The function maps the coordinates of the flow front profile shape and then finds

the locations (with respect to the x-axis) of the trailing edge, leading edge, and average profile position. This was accomplished by applying additional filtering to yield a binary image that simply highlighted the flow area (upstream from the front) and the non-flow area (downstream from the front), an example of which is illustrated in Figure 3-6B. The flow front position data resulted from analysis of this simplified binary image, which data included the coordinates for the actual profile shape as well as the locations for the trailing edge, leading edge, and average position of the profile. The simplified binary image was discarded, and the flow front positions were passed back to the main program, to be later used in conjunction with RIA void calculations.

Figure 3-6: Different Stages of the Binary Image Conversion Process

With the flow front position known, the final image conversion steps focused on filtering out non-void pixel groups from the binary image. Code developed by Kimberly Stevens and Caleb Lystrup (Stevens, 2018; Lystrup, 2018) was incorporated to accomplish this by limiting

the minimum and maximum allowed pixel region sizes. A minimum threshold was set to account for things like camera sensor noise or dust on the lens which could manifest as pixel noise in the binary image. The maximum threshold primarily was to eliminate the large regions that were actually a result of the fiber tows pressing up against the acrylic mold, and not voids or bubbles. The largest white regions seen in Figure 3-5D and Figure 3-6A illustrate this type of noise. The eccentricity filter was applied last as a means of controlling similar such noise, but for smaller tow areas or stitch threads with minor pixel areas but very linear shapes.

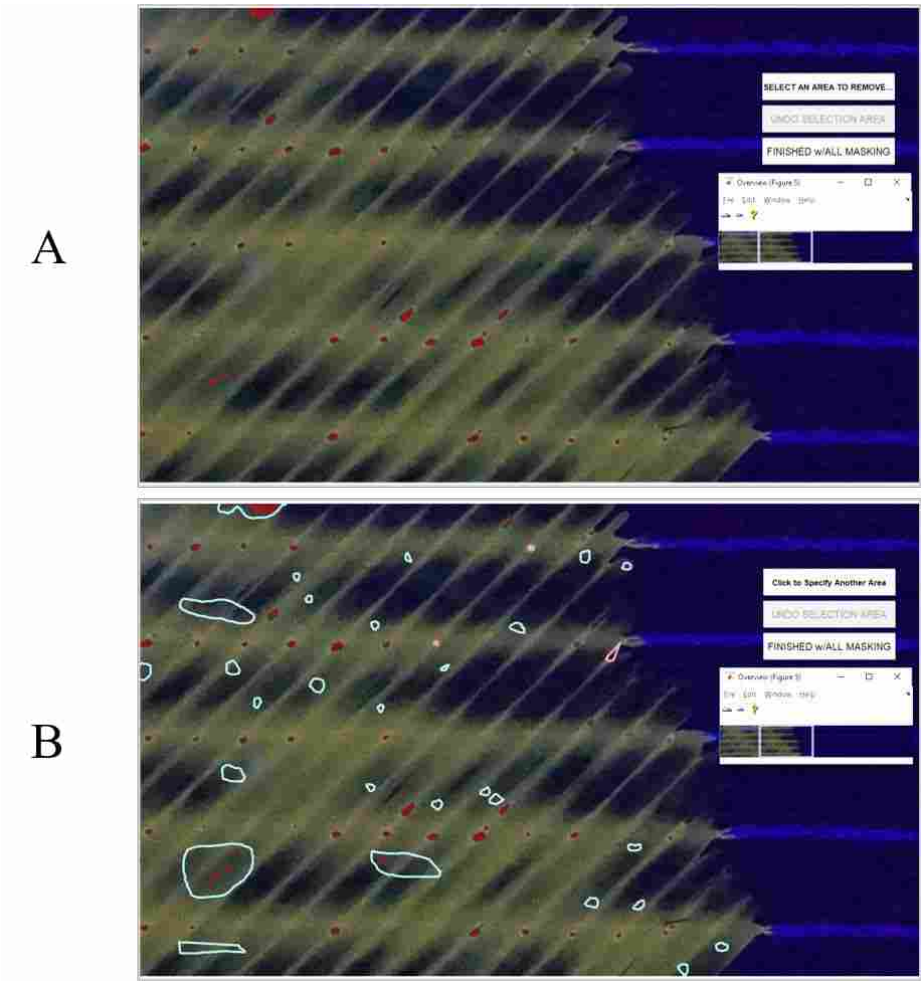

Figure 3-7: Screenshots of the Manual Editing Process for Binary Images Within MATLAB

Any remaining pixel regions were then filled to eliminate "holes" – areas of black pixels that are fully encircled by a single, connected region of white pixels – and then underwent a final, user-involved step: the binary image was superimposed (as a semi-transparent red color) onto the original source photo to allow for a final double-check and edit of results. Screenshots from this process are shown in Figure 3-7. Image A shows the initially-filtered binary image superimposed on the full color source image to allow for user evaluation. After evaluating the current state of the binary image, the user had the option to manually remove or add specific pixel regions, which was done for each area of interest by drawing a boundary and then specifying whether that area should be added to or removed from the binary image. An example of this step is shown in Figure 3-7B. Once all the manual edits were defined the binary image was updated. This was its final state. Figure 3-5E and Figure 3-6C are examples of such binary images. This binary image result was then passed through to the remainder of the program's processing loop for void content measurement within the different pre-defined RIA boundaries.

3.7.2 Representative Image Area Determination

As noted above, the entire image was not considered in void measurement but instead was limited to an area of the preform as defined in MATLAB. The present study focused its analysis on the centered 50% of the preform width, according to the following.

Although the void measurement methodology is semi-automated, the accuracy of the analysis is still improved by user correction of incorrectly identified voids as well as missed voids in each binary image. This takes some time per image, so with the large volume of images analyzed it was decided to focus on a strip narrower than the entire width of flow front to decrease the time of analysis and improve overall accuracy of results. The overall area analyzed

consisted of the middle 25 mm of the entire 50 mm sample width and ran the full 300 mm length of the preform. It should be noted that a commonly discussed weakness of unidirectional flow testing is its susceptibility to race-tracking, in which the variation in edge-sealing tightness or preform geometry can cause either slower or faster flow along the edges compared to the middle of the reinforcement sample (Bickerton, 2000; Brandley, 2016; Richardson, 2000). As mentioned above, strategic use of a moveable silicone gasket seal aimed to mitigate some of this race-tracking risk. Disregarding 50% of the available experimental image area from analysis had the added benefit of eliminating much of the influence from race-tracking effects along the sample edges.

Boundaries for each RIA, i.e. the regions in which void content was to be considered, were specified for all images according to the following. The choice of RIA length, i.e. how far back from the flow front to consider in the analysis, was less intuitive than choice of width. Flow-induced bubble formation is expected to occur immediately at the flow front, and bubbles immediately begin to evolve in shape, size or position. Thus, the most accurate depiction of bubble formation would focus only on the immediate flow front. In practice, this is hindered by the evolution of nonlinear flow front profiles, and by the fact that the bubble shapes are not points in space at the flow front edge but actually shapes which extend back and away from the flow front. Thus the RIA must extend back a distance from the flow front to capture the area of bubbles being formed. But the longer the RIA length, the more probable that bubbles observed in the analysis have changed in size, shape, or position since their formation. Previous studies with similar work give few recommendations on the topic (Lystrup, 2018). Thus several RIA lengths were employed during analysis: the entire flow area length (variable due to the fixed camera

position and changing flow front position), 20 mm, 40 mm, and 60 mm – all being measured upstream from the trailing edge of the flow front.

Two additional RIA lengths were defined with a different strategy: the leading edge boundaries of these RIAs were curved to match the flow front profile shape, and then that same profile shape was translated upstream by a distance of either 20 or 40 mm and used as the trailing boundary edge shape (Figure 3-8). A comparison of results for these different RIA length choices will be presented later.

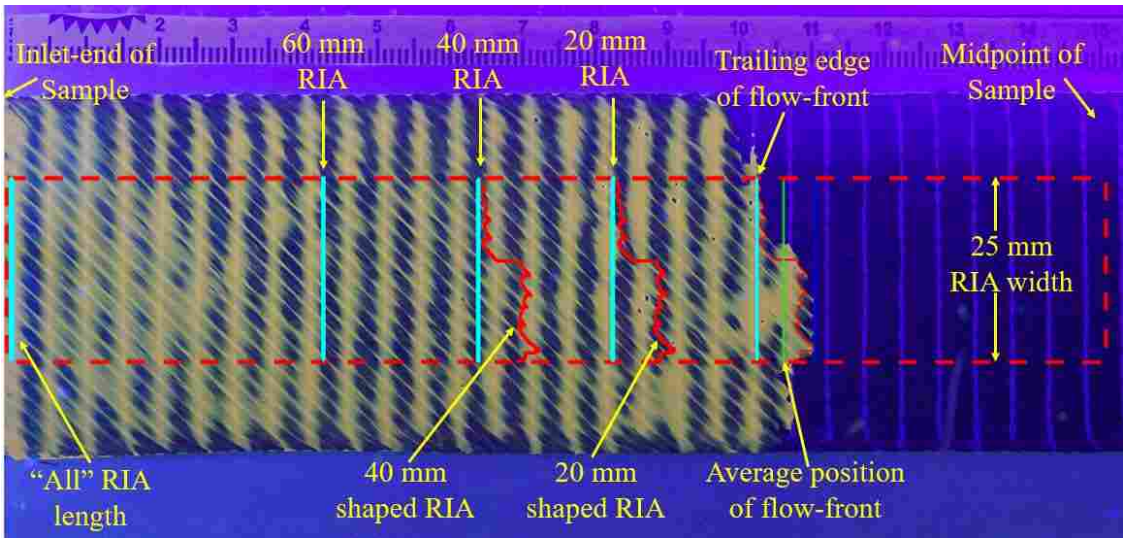

Figure 3-8: Illustration of Flow Front and RIA Width and Length Determination

As the boundaries for each RIA were defined in MATLAB, subsequent void analysis considered only the pixels within the given area(s). The program accomplished this by masking off all non-RIA area for a given binary image, and then proceeding with v_0 calculations. Within each given RIA the v_0 value was obtained by comparing the number of void pixels (white regions) with the total number of pixels present. Other types of pixel-based void measurements

(such as void size, nearest neighbor distance) were considered but ultimately were not implemented within the scope of this study.

The same RIA boundary values were specified and applied for all images analyzed in this study. The various RIA v_0 data points were calculated and indexed for each of the binary images obtained from the image conversion process described earlier. Once all images in a sequence had been converted to binary and analyzed for void content then all the RIA data points for all images were compiled and output by MATLAB. These results were then imported into Microsoft Excel for further organization and analysis, the results of which are given in the following chapter.

4 RESULTS

4.1 Qualitative Analysis

Capturing images at a regular time interval proved very useful in visualizing bubble movement and areas of bubble entrapment or accumulation. Bubble flow in the NCF was noticeably affected by stitch geometries, which was true for infusions done with the stitching oriented in the 90° direction (T1, T2) and 0° direction (T3). At times void formation was influenced by capillary action wicking fluid into the stitching ahead of the main flow front (as is illustrated in later figures; see section 4.2.4). But when the bulk flow (marked by the progression of the general flow front profile edge) was only slightly trailing behind the capillary flow in the stitching, no such influence on void formation was observed. It should be noted that the work of this visualization study focused primarily on characterizing flow front formation (and subsequent migration) behavior of macro-voids. The following discussions of image data and results refer to these such inter-tow bubbles.

Regardless of how stitching may have affected bubble formation (at the flow-front), in all cases it was observed that post-formation movement of formed bubbles was strongly affected by the stitch geometry. It was observed that bubble flow often followed a stop-start migration pattern around the stitch lines, i.e. formation was often followed by a short migration which would then cease when the bubble encountered stitch thread geometry. This occurred in both the 90° and 0° infusions of the NCF, as the bubble flow proceeded along the inter-tow gaps which

were in the bias (45°) direction relative to the flow direction, thus bubbles could meet stitch lines both parallel and perpendicular to the flow direction. This behavior was evidenced by the regularly-spaced voids observed in images from all the NCF infusions, as seen in Figure 4-1. In the raw color image shown in Figure 4-1A a few examples of the stitching fiber are labeled and marked with pink, dashed lines. The fluid flow direction is indicated with the black, labeled arrow. Figure 4-1B shows the associated binary image, with bubbles shown in white. Red arrows indicate the aforementioned regular, stitch-influenced spacing between void areas.

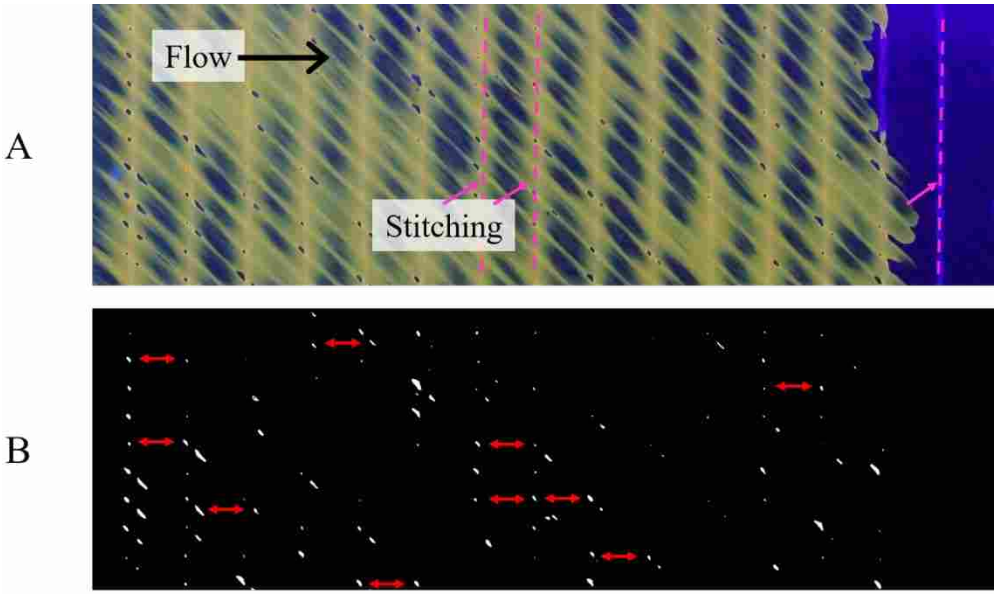

Figure 4-1: Example of Regularly-spaced Voids Observed in Stitching Areas

Many of the formed bubbles were initially stationary as the flow front passed by, remaining in either the place where they were formed or where they first got stuck (usually on stitching) immediately after being formed. As the infusion proceeded, the bubbles would slowly shrink in size by the Ideal Gas Law as the local fluid pressure increased, and either disappeared as they were dissolved into solution, or escaped their confinement and usually proceeded rapidly

toward the flow front. This observed bubble behavior agrees with the expected pattern that has been described in previous studies (Lundstrom, 1993; Gourichon, 2006; Patel, 1996), in which the successive bubble migration event(s) only occur after the flow front has traveled a sufficient distance downstream and the increasing resin pressure effects a reduction in bubble size such that further movement is possible.

Bubble flow in the STW plain weave fabric (T4 through T7) was more complex than that observed in the NCF infusions. The preform configuration proved to be very dense, requiring higher pressures for constant injection velocity. This ultimately meant that the injection machine would reach the maximum-allowable pressure very early into the infusion and so the remaining majority of the test was then carried out at constant pressure. Specific aspects of permeability are discussed in more detail later. The binder found on the surface of this fabric appeared to have a similar influence on bubble migration as did the stitching for the NCF in tests T1 through T3, namely it was seen to hinder and/or direct flow of bubble migration. This was evident from the location of immobile bubbles relative to the binder. Figure 4-2A shows an example image from T6 where bubbles formed at the flow front became trapped against the binder geometry. Red arrows indicate specific areas that show newly-formed bubbles that appear trapped (or at least temporarily stuck) behind binder material. For clarity, the same image is repeated in Figure 4-2B with a portion of the binder material and voids highlighted in white and yellow, respectively.

A frame-by-fame qualitative evaluation of bubble formation and entrapment was performed. In areas with more-regular binder bead geometry (i.e. geometry with smooth, continuous arcs) there appeared to be fewer discreet bubbles present, though the size of these tended to be larger than those trapped in areas with irregular (i.e. “messy”) binder patterns. This could be due to easier migration for bubbles that move alongside smoother, regular binder paths.

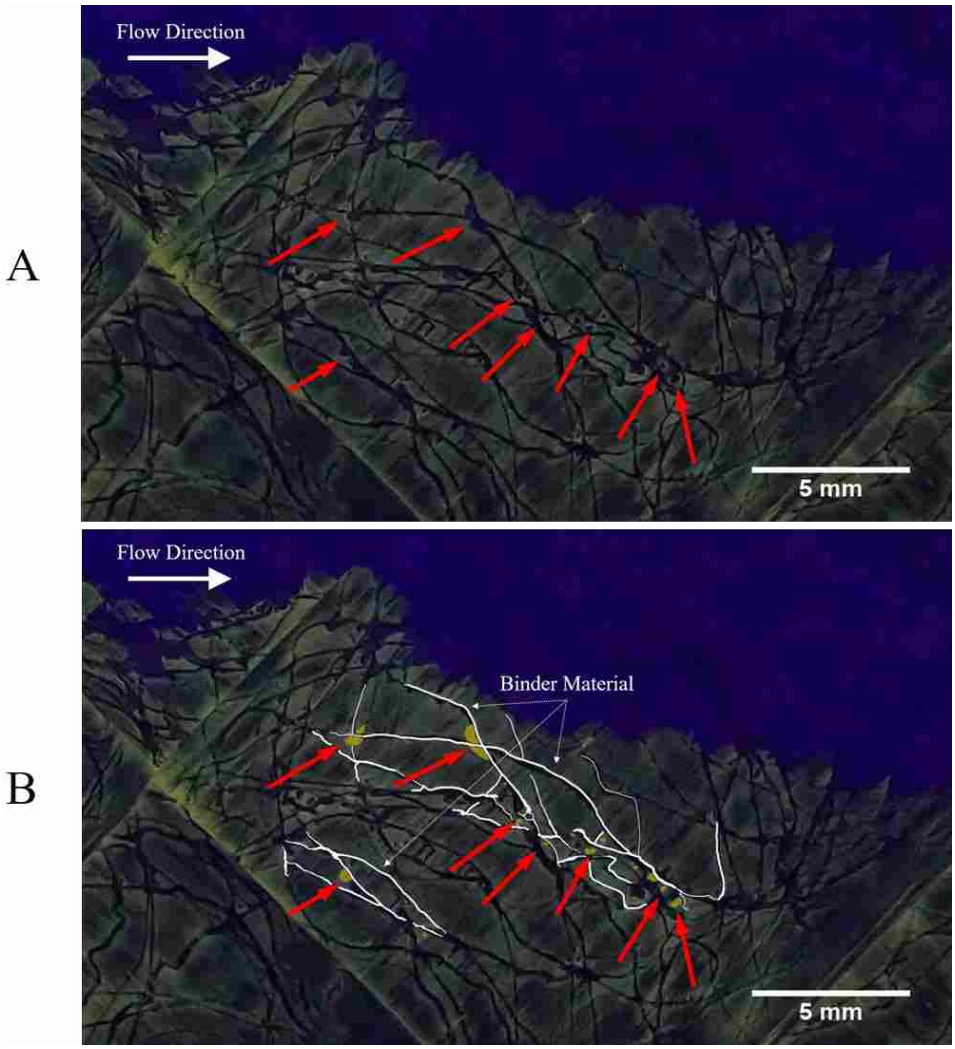

Figure 4-2: Bubble Entrapment Related to Binder Geometries in STW Fiber Architecture

Bubbles would collect and coalesce in the furthest-forward position within a given binder boundary area. Naturally, migration along irregular binder paths would slow or stop bubble movement and thus reduce the probability of bubble-to-bubble interaction and merging. These binder-related migration observations are illustrated in images from T6, as shown in Figure 4-3 and Figure 4-4. In Figure 4-3 the red arrows indicate the locations of bubbles, which appear trapped behind the arc-shaped bead of binder material indicated by the dotted red line. Figure 4-4 shows the different patterns of binder bead geometry present in the STW fabric used in this

study. Visible in the upper and lower portions of the image detail are the more-uniform binder bead pattern (i.e. “clean” geometry) and irregular (“messy”) binder patterns, respectively. Note the relatively low number of discreet bubbles seen in the “clean” binder geometry compared to the “messy” binder patterns.

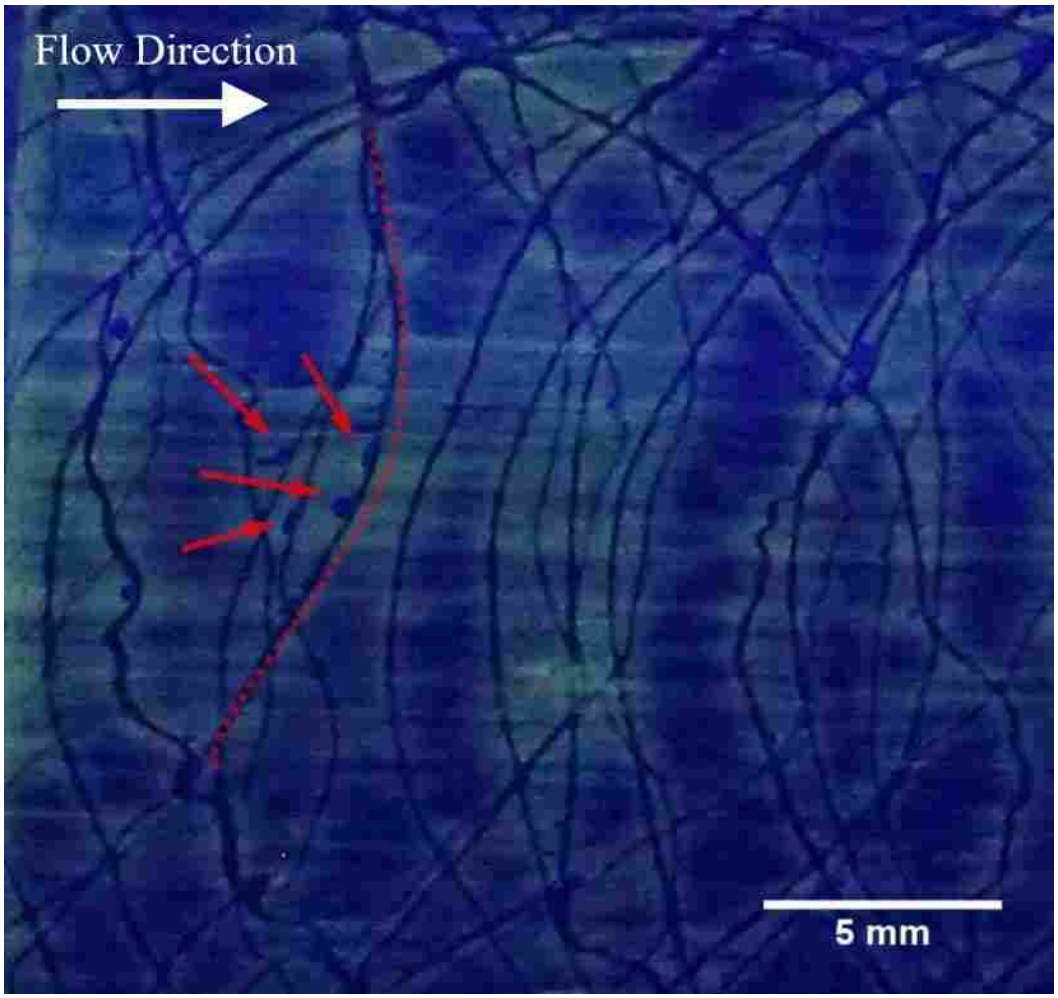

Figure 4-3: Bubbles Migrating and Collecting Behind an Arc-shaped Bead of Binder

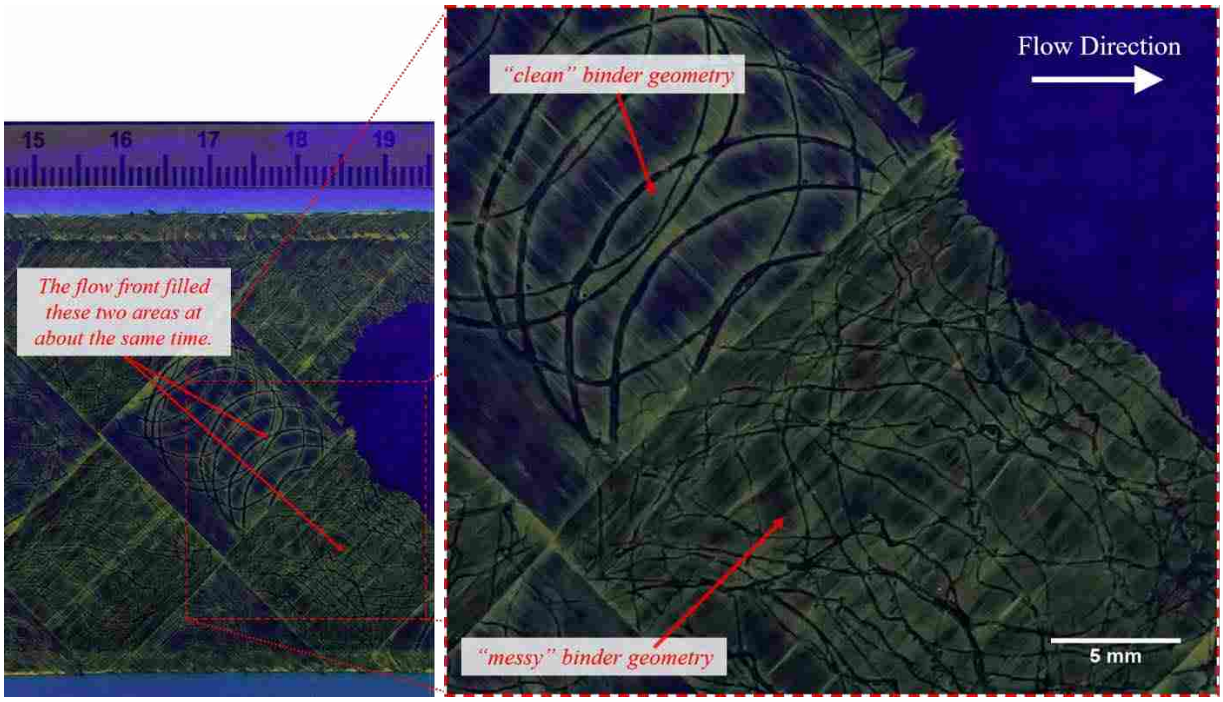

Figure 4-4: Image Detail for Comparison of Regular and Irregular Binder Bead Geometries

The MATLAB analysis method developed for batch analysis of image sequences for void content (v_0) did not prove very effective for the images from tests T4 through T7. The size of bubbles seen during the tests with the Oxeon STW fabric proved to be on the extreme end of what was measurable with the obtained pixel per mm resolution, increasing the sensitivity with respect to camera lens focus error and lighting conditions. Because the infusion was done at constant pressure, and because the fiber stack was so dense, overall bubble velocity (speed of migration) was slow and, due to the binder geometry and plain weave fabric architecture, constantly interrupted. The irregular width and location of the binder lines did not allow for a simple blanket application of high pass / low pass filters values across all sequence images (the strategy typically employed to remove non-void pixel regions). Filtration by color segmentation of the source image was not effective as the binder appeared to be the same color as the voids, likely due to it pressing against the underside of the acrylic mold top. Small bubble size, irregular

binder geometry, similarity in binder and bubble color, and increased sensitivity to lens focus error – all such factors detracted from the quality of MATLAB results. Error in determining the discreet boundary lines between regions would yield inaccurate binary images that had entire regions missing or (as was often the case) inaccurately combined with other pixel areas. Consequently, no valid void measurement data for the Oxeon STW plain weave fabric (T4 through T7) was collected via MATLAB. Infusions T4 through T7 are excluded from consideration in all quantitative results and analysis presented in the next section (4.2) unless otherwise noted. Future work will attempt to mitigate these problems and allow bubble identification and quantification. But for the present study, quantitative analysis is only done on the NCF reinforcement.

4.2 Quantitative Analysis

4.2.1 RIA Length and Shape Comparison

As mentioned in Chapter 3, several RIA lengths were employed during analysis: the entire flow length from current front location upstream to start of the preform (variable due to the fixed camera position and changing flow front position), 20 mm, 40 mm, and 60 mm from the trailing edge of the flow front, as well as 20 and 40 mm with the upstream and downstream boundaries curved to match the shape of the flow front's edge profile. In an effort to simplify data analysis and discussion, an initial analysis was performed to determine how these RIA data set(s) and their respective trends might differ from one another in their representation of the experimental results. Figure 4-5 shows the results of plotting the measurement of void content (v_0) by each of the available RIA choices with the instantaneous flow front velocity (v). The method employed to determine v for each image is detailed in a later section (0). Data for T1 and T2 are shown in

plot A and plot B, respectively. (There was no significant patterns observed for the equivalent $v_0(v)$ RIA data from T3, which is discussed in a later section.) For this analysis the individual image data points for each RIA were aggregated into data bins with respect to v, the average value of v_0 was calculated for each bin and then graphed at the v value which represents the center of the bin range. Power law fits were then applied to each RIA dataset, which show that all RIAs exhibit similar trends in $v_0(v)$. Table 4-1 lists the bin boundary values used to aggregate the RIA data which is shown in Figure 4-5.

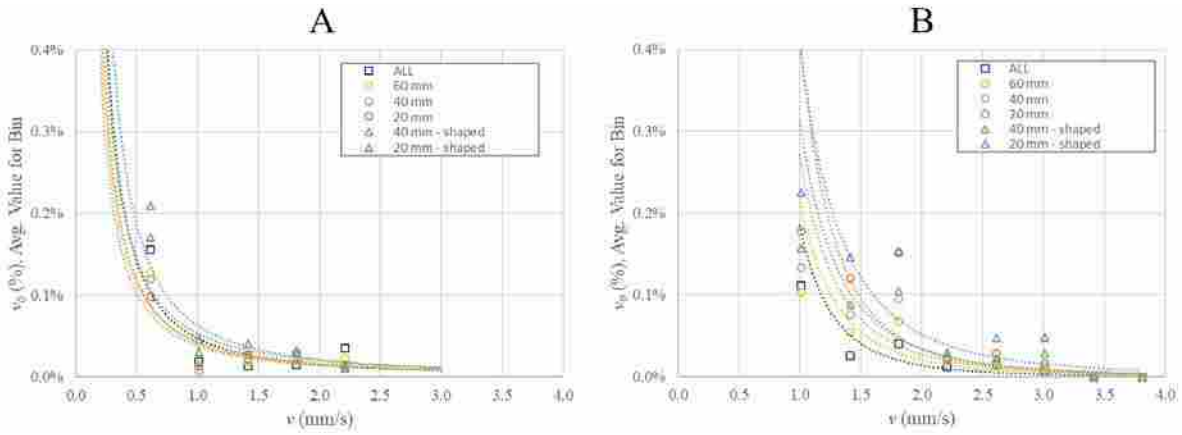

Figure 4-5: Comparison of $v_0(v)$ for Different RIA Length and Shape Choices

There has been no consistent discussion in the literature as to what type of curve fit is to be expected with $v_0(v)$ trends, as was previously discussed with Figure 2-1. Throughout this study a power law curve was considered with the experimental data per it generally had the best fit to the $v_0(v)$ results, compared to other curve options, when considering individual (non-averaged) datapoints. To remain consistent, power law trendline fits were also used for the other presented results (and generally had good fit, compared to alternative function types such as linear or exponential). Allowing the experimental results to dictate the applied curve fit is a strategy

Table 4-1: Bin Boundaries for Velocity Data, Used in RIA Data Aggregation

Bin #	*Lower Boundary Value (mm/s)*	*Center Value in Bin Range (mm/s)*	*Upper Boundary Value (mm/s)*	*Bin Range (mm/s)*
1	0.0	0.2	0.4	0.4
2	0.4	0.6	0.8	0.4
3	0.8	1.0	1.2	0.4
4	1.2	1.4	1.6	0.4
5	1.6	1.8	2.0	0.4
6	2.0	2.2	2.4	0.4
7	2.4	2.6	2.8	0.4
8	2.8	3.0	3.2	0.4
9	3.2	3.4	3.6	0.4
10	3.6	3.8	4.0	0.4
Bin Assignment Rules: Lower Boundary ≤ v < Upper Boundary				

established in the relevant literature (Park, 2011). Further discussion of overall $v_0(v)$ results is given in section 4.2.3.The fit equations and R^2 values for the power law trends of the different RIAs shown in Figure 4-5 are listed in Table 4-2. The $v_0(v)$ data shows good fit with power law trends in the case of RIA data from T1, with a decrease in void content across all RIAs observed with increasing velocity. The T2 data shows a similar decrease in v_0 with increasing velocity, with acceptable (though somewhat weaker) fits to power law curves. Little difference between the curve fits for the different RIAs is first observed. The RIAs for a given infusion all show similar R^2 values to each other, which is inferred to mean that the dataset for any given RIA could represent the general trends associated with $v_0(v)$ about as equally well as any of the other RIA datasets from that experiment.

Table 4-2: Power Law Fits for the $v_0(v)$ Data of Each RIA in T1 and T2

Test	*RIA*	*Best Fit Equation*	R^2 *Value*
T1	"All"	$y = 4.73E\text{-}04x^{-1.59}$	0.807
T1	20 mm	$y = 4.14E\text{-}04x^{-1.52}$	0.850
T1	40 mm	$y = 3.78E\text{-}04x^{-1.44}$	0.756
T1	60 mm	$y = 4.27E\text{-}04x^{-1.43}$	0.814
T1	20 mm "shaped"	$y = 6.28E\text{-}04x^{-1.57}$	0.948
T1	40 mm "shaped"	$y = 5.32E\text{-}04x^{-1.43}$	0.931
T2	"All"	$y = 1.85E\text{-}03x^{-3.76}$	0.77
T2	20 mm	$y = 4.17E\text{-}03x^{-3.63}$	0.67
T2	40 mm	$y = 2.71E\text{-}03x^{-3.32}$	0.83
T2	60 mm	$y = 2.17E\text{-}03x^{-3.43}$	0.83
T2	20 mm "shaped"	$y = 4.10E\text{-}03x^{-2.99}$	0.62
T2	40 mm "shaped"	$y = 3.12E\text{-}03x^{-3.22}$	0.77

Upon closer inspection, the profiles in Figure 4-5 follow logical trends in relation to the RIA length. One would expect the shorter RIAs to result in the highest measured void content (and, possibly, better fit to the curve), as there are fewer voids the farther back from the flow front one looks, i.e. the fluid pressure increases upstream of the flow front, causing bubbles to shrink in size by the ideal gas law and eventually dissolve into solution by Henry's Law. When upstream and downstream boundaries followed the flow front shape a slight increase in v_0 was measured, compared to the RIA of the same length measured with straight upstream and

downstream boundaries. This is also to be expected, as the straight line RIA shape considers the upstream area beginning from the position of the trailing flow front edge, and thus analyzes some locations farther back from the flow front than in the shaped front RIA (which considers the upstream area starting from the actual flow front profile shape).

RIA length and shape thus influences the void content measurements. The shorter the RIA length, and the more it follows the true flow front shape, the more representative the measured v_0 is of the void formation at the flow front. Shorter RIA lengths are also expected to cause more scatter in results, though. This is due to the imperfect spacing of the voids; although periodic in nature (Figure 4-1), void formation does not appear to occur in a perfectly spaced pattern. It is only a higher probability that a void will be formed or become stuck at each of the stitch line crossovers, and not a guarantee. Images which showed large lag distances between the leading and trailing flow front edges were more difficult to process with the MATLAB software that was used to find the front location, a factor which also could influence the accuracy of void content measured for the shorter RIA lengths as any error in locating the flow front profile would be more apparent when considering a smaller overall area. As a compromise between these choices in RIA length, and with consideration for the aforementioned factors and R^2 values for T1 and T2 in Table 4-2, all presented void analysis in the rest of this study is done with the data from the 40 mm long "shaped" RIA, which has leading and trailing boundaries shaped to match the flow front curvature.

Unless otherwise stated, for all void content analysis presented in this paper the individual v_0 data points were only included in a given RIA for images in which the flow front position had reached a position far enough to allow for a full area fraction calculation. E.g. if the flow front was at a position of 30 mm in a given image then no data point would be considered for the RIA

with the boundary set 40 mm upstream from the front. Thus in Figure 4-5 only the data points from images with an acceptable size upstream area were included in the respective aggregated RIA data sets shown.

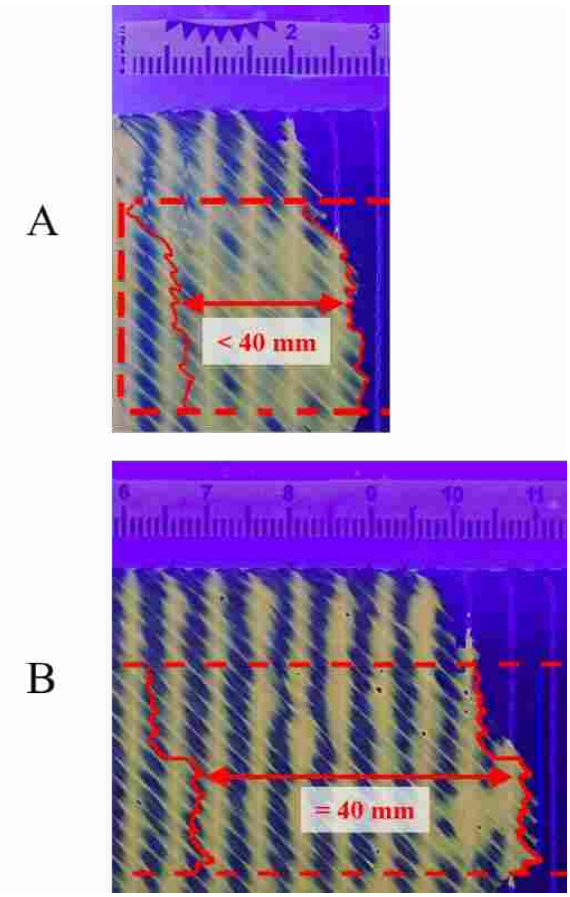

Figure 4-6: Example Images of Incomplete ("Short") and Acceptable Analysis Areas

The concept of acceptable upstream area for RIA analysis is illustrated in Figure 4-6, which is shown with consideration for the 40 mm RIA with the "shaped" upstream and downstream boundaries. Image A illustrates an example case of a "short" RIA, where the upstream boundary fails to meet the full 40 mm offset distance from the flow front. Thus void data from image A

would be excluded from consideration with respect for the 40 mm RIA (but could still be included in the dataset for the 20 mm RIA). Image B illustrates an acceptable RIA case, where the specified area behind the flow front is fully-available for inclusion in the area calculations. The resultant data point from image B would be considered during data analysis with the 40 mm shaped RIA.

4.2.2 Flow Front Position and Velocity Determination

Ideally, in a unidirectional flow test such as these, the flow front would be linear and perpendicular to the flow direction. In practice, however, the textile architecture does not follow any perfect unit cell model and instead exhibits some degree of micro-variation in architecture (Pan, 2000; Lundstrom, 2000; Loendersloot, 2006). This micro-variation, along with the previously-mentioned phenomenon of race-tracking, caused small deviations from linearity in the flow front shape for each experiment. When restricting the RIA to a 25 mm wide strip along the flow front width (i.e. in the direction of the preform width, transverse to the direction of flow,) this nonlinear deviation is minimized, yet there was still a measurable difference between the front edge of the flow front and the trailing edge in each image. To mitigate any effect on subsequent analysis caused by this difference, the distance of the average flow front position from the preform start L was calculated during image analysis for each of the images. This is illustrated in Figure 4-7. The white arrows are an illustrative representation of how the perpendicular distance from the preform start to each individual pixel along the flow front profile was measured parallel to the flow direction. The average of the individual pixel measurements is what gave the overall average flow front position distance from the preform start (L), represented in the figure by the yellow line. The solid and dotted red lines represent the flow front profile and the RIA 25 mm width boundary box, respectively, as explained in Figure 3-8. Note that though

the figure depicts L as a distance it is also referred to as a position throughout the discussion presented in this work.

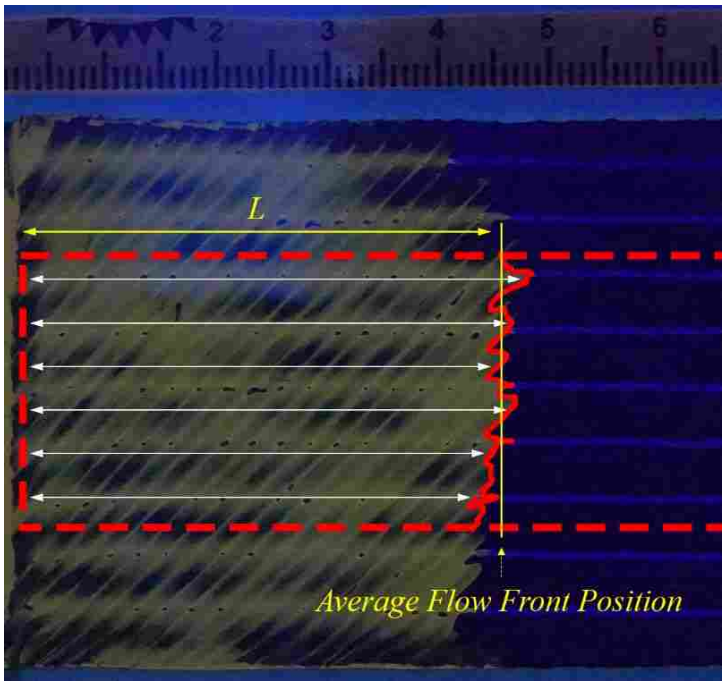

Figure 4-7: Illustration of Average Flow Front Position

The instantaneous flow front velocity v for any image was determined from a 2-point average flow front position L and time t differences for the image before and the image in question, as shown in Equation 4-1:

$$v = \left[\left(\frac{L_i - L_{i-1}}{t_i - t_{i-1}}\right) + \left(\frac{L_{i+1} - L_i}{t_{i+1} - t_i}\right)\right]/2 \quad (4\text{-}1)$$

The time t for each image was determined from the time stamps on each image file.

The flow front velocity (v) is compared in Figure 4-8, for the case of calculation by 1) the average and 2) trailing edge methods of flow front position determination, represented by solid and hollow symbols, respectively. Data in the figure is from T1, T2, and T3. This figure is

presented to show that the function $v(L)$ velocity seems to change little in shape or magnitude between the two methods, although the trailing edge method seems to give more scatter in results. Thus, the average flow front position is used for analysis throughout the remainder of this paper unless otherwise noted, with L considered as shown in Figure 4-7 .

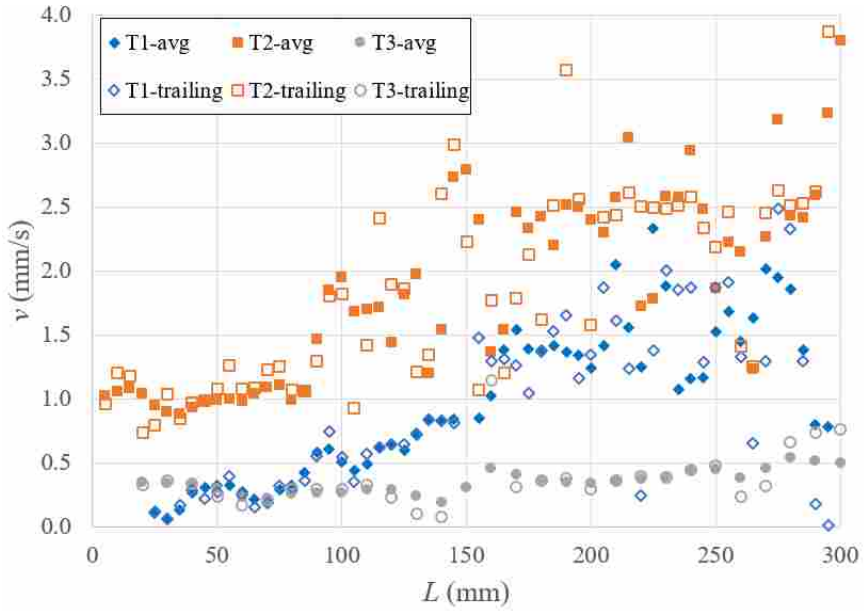

Figure 4-8: Flow Front Velocity Calculated from Average and Trailing Edge Position Data

The cause of the variation in flow velocity shown in Figure 4-8 is unclear. As previously described in the methodology, with using a constant-displacement RTM machine the initial expectation was that the observed resin flow velocity would be relatively constant for each test infusion. Figure 4-8 clearly illustrates that this was not found to be the case, as variation in velocity exists within the dataset of each test infusion considered.

Further investigation into this included consideration of the pressure data from the infusions. Figure 4-9 shows the correlation of the pressure measurements for the RTM machine sensor and the dedicated pressure sensor on the fluid inlet line. The data in the figure is from T1,

T2, and T3. It is clear that the pressure sensor on the RTM machine had little-to-no correlation with the measurements from the dedicated pressure sensor on the line by the tool inlet. This is most likely due to low resolution associated with the pressure and flow sensors for the RTM machine. Although various flowrates (Q) were specified in the machine settings, the values used in this study were on the very lowest end of the specifiable range for the ISOJET machine, as typical industrial manufacturing involves larger mold cavities to fill. This suggests that the displacement measurement and/or control are not fine enough resolution to effectively achieve these low Q values. Accordingly, the pressure sensor on such a machine is only expected to be a low-resolution device which serves as safety check to ensure the system does not exceed the maximum allowable pressure – not a high precision measuring device as is typically used for flow modeling experiments.

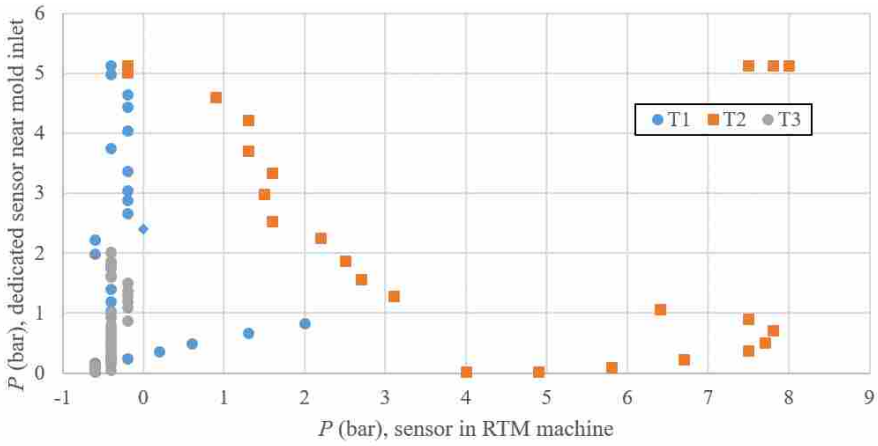

Figure 4-9: Correlation of P Measurements for Pressure Sensor in RTM Machine and Dedicated Pressure Sensor on Fluid Inlet Line

Thus the pressure measurements and flowrates recorded by the RTM machine were discounted and instead the dedicated pressure sensor measurements were evaluated along with

the flow front velocity (which was calculated via the flow front position measurement data obtained during the MATLAB image analysis).

For a constant flow rate experiment it is anticipated that both flow front position and inlet pressure with increase linearly with respect to time. Figure 4-10 illustrates the pressure and length histories for all seven test infusions. The STW reinforcement configuration (T4 through T7) proved to be denser, i.e. lower permeability compared to the NCF (T1 through T3), as shown by the relatively higher pressures and fill times in Figure 4-10B. The pressure maxed out in all of the STW infusions at the 8.5 bar safety limit set on the injection system, and thus proceeded as a constant pressure infusion thereafter. In comparison, the pressure never hit the 8.5 bar limit for the NCF infusions, even at the highest flow velocity in T2.

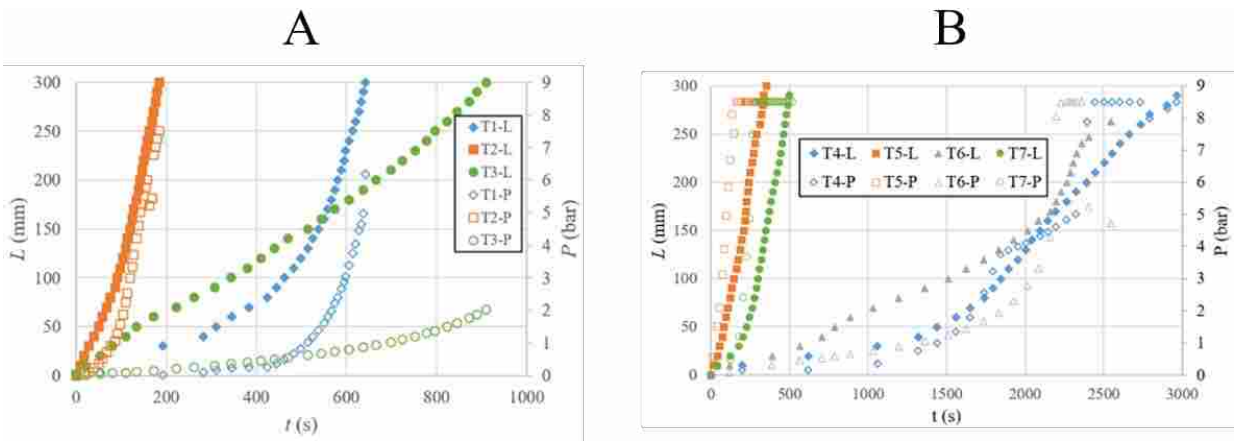

Figure 4-10: $L(t)$ and $P(t)$ for T1 through T3 (A) and T4 through T7 (B)

Permeability of the fiber preform configurations was investigated to see if there was any obvious cause that could be established as to why the flow front velocity varied during each infusion as shown in Figure 4-8. One might expect to see an increase in measured permeability for flow front positions with higher instantaneous velocity measurements, but the results in

Figure 4-11A show that for T1 through T3 (the NCF infusions further-analyzed for void formation) there was no apparent jump in K which could be construed as cause for the variation in v that is seen around L of ~100 mm in Figure 4-8. Data for T4 through T6 (infusions done with Oxeon STW plain weave fabric) are shown in Figure 4-11B to illustrate the difference in permeability as compared with the NCF infusions.

As with any such tooling setup, the permeability of the reinforcement in a given image may be calculated with Darcy's Law when the inlet pressure and flow front position data are known. Figure 4-11 below illustrates the permeability (K) as calculated by Darcy's Law:

$$K = \frac{v\varphi\mu L}{\Delta P} \tag{4-2}$$

for the instantaneous velocity (v) at the flow front location L for each image analyzed. In this equation, φ, μ, and ΔP represent the reinforcement porosity (1-v_F), test fluid viscosity, and pressure gradient (inlet to flow front), respectively. As seen in Figure 4-11, the data is only represented for flow lengths up to 200 and 150 mm for the NCF and the STW, respectively, due to the onset of slight race-tracking at approximately these locations causing gradually increasing permeability for the subsequent downstream areas beyond. Over this shortened range of data, the calculated average permeability for the NCF at this fiber content (54%) was

$2.79 \pm 0.62 \cdot 10^{-11}$ m^2.

The variation in permeability through an experiment can be considered a measure of the extent of race-tracking during an infusion. Assuming constant mold thickness and viscosity, the velocity should be proportional to $\Delta P/L$ (Equation 4-2) and the permeability a constant value for a given reinforcement. The permeability is thought to be a function of the fabric architecture alone, and thus a significant change in the measured permeability through such an experiment

may suggest race-tracking, where the flow now travels through a preferential channel instead of through the reinforcement itself. In Figure 4-11A, the NCF infusions demonstrate a high and variable measured K, but then seem to settle to more or less constant values, suggesting little race-tracking. Such initial variation in permeability is common due to flow entrance effects and the short time required for the applied pressure to stabilize within the filled area by the inlet.

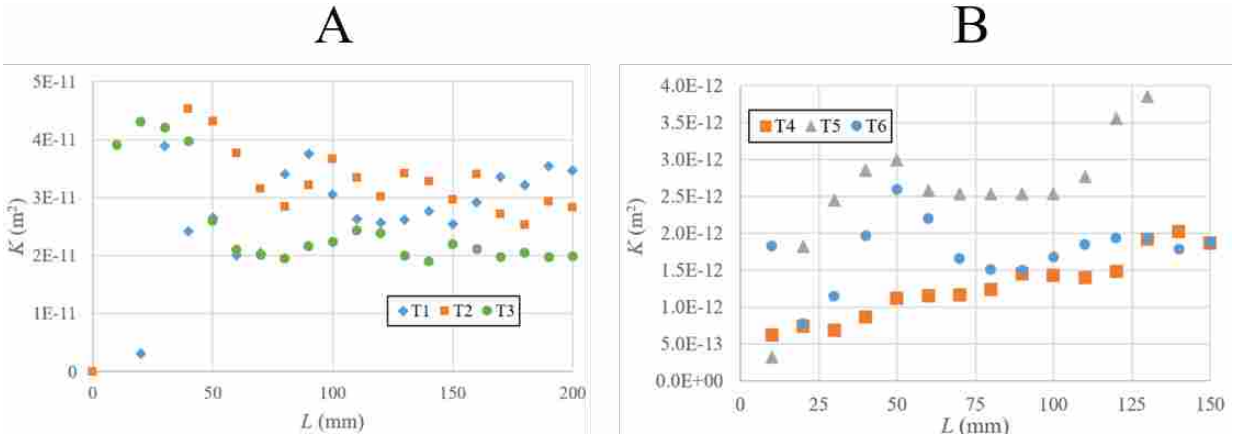

Figure 4-11: $K(L)$ for T1 through T3 (A) and T4 through T6 (B)

The STW infusions (Figure 4-11B) also show an initial variation in K, then stabilize between 50 and 100 mm, then rise at the end. This suggests that there is a degree of race-tracking occurring towards the end of these infusions. It is likely that this more pronounced edge flow effect was influenced by the lower permeability of the STW plain weave preform (Richardson, 2000).

The permeability was not calculated for T7 due to the pressure sensor measurements being incomplete for that infusion. The average permeability over the other three STW plain weave experiments (T4 through T6) was calculated to be $1.77 \pm 0.64 \cdot 10^{-12}$ m^2. This value was then used in combination with Darcy's Law (Equation 4-2) to predict the pressure gradient through the T7 experimental duration that is shown in Figure 4-10.

4.2.3 Void Measurement Results

As mentioned in section 4.2.1, the void data considered in the results analysis is from the RIA with the shaped boundary 40 mm upstream from the flow front. As was done for Figure 4-5, any v_0 data points for flow front positions which did not allow the RIA boundary to be translated the full 40 mm upstream (i.e. when the flow front was at a position less than 40 mm from the inlet, or when considering the first few images from the camera that captured the second half of the preform length) were excluded from consideration for the figures shown in this section (Figure 4-6A).

Figure 4-12 shows the results for void measurement plotted with the flow front position L for each of several photographs during the infusions T1, T2, and T3. This data was evaluated for any obvious outliers or interruptions in the general void content trend across the length of each infusion, as such could signify issues with an individual datapoint or the entire infusion. The observed trends look to be as expected. The void content in each image's RIA close to the flow front is under 1% (except for a few T1 images close to the inlet, but those were excluded from consideration per the example shown in Figure 4-6A). Generally higher void content was observed in the 0° infusion (T3) than the 90° flow tests (T1 and T2). The data in Figure 4-12A is repeated in Figure 4-12B, with the y-axis viewed with a logarithmic scale to better observe the very low void content results from photographs towards the mold vent. A decreasing relationship can be seen in the data for T1 and T2 (the 90° infusions). The power law fit for T1 (R^2=0.486) was slightly weaker than that of T2 (R^2=0.550). The T3 0° infusion results seem to be decreasing over the length of the infusion as well, although there is a dip in measured void content from 50 to 100 mm, followed by a more gradual decrease in void content than that in T1 and T2. The lack of a notable power law fit for the T3 data suggests there is not the same type of trend as seen for

T1 and T2. Comparing the similar shapes of the profiles for T1 and T2 with the differing shape for T3 also supports the idea that void formation is significantly different in the two flow directions. It is also inferred that if bubble migration is a contributing factor to the observed difference then it is likely related to stitching orientation, as all NCF infusions had the same principle fiber orientation with carbon tows at +/- 45° relative to the flow direction. But the flow velocities in each of these infusions are also significantly different, and velocity is the variable to which the void formation rate is commonly related. Thus the following analysis considers the relationship of flow velocity and void content.

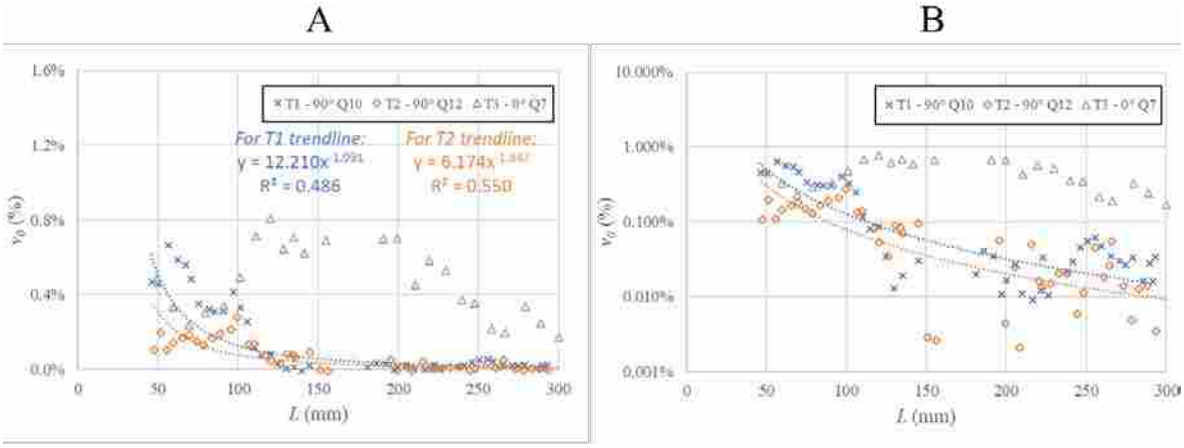

Figure 4-12: $v_0(L)$, with Power Law Fits Shown for T1 and T2

Figure 4-13 illustrates the measured void concentration data plotted as a function of the measured instantaneous flow front velocity for each analyzed image. Power law fits for T1 & T2 (combined dataset), and T3 are shown; Plot B is the same as A, but with a logarithmic Y-axis. The power law fits and R^2 values associated with $v_0(v)$ can be found in Table 4-3. A decreasing trend in this data agrees with the general expected trend discussed in the literature (shown in Figure 2-1), and is similar to trends seen by previous researchers (Patel, 1996; Lystrup, 2018).

Note that some studies have shown a further increase in void formation at higher velocities (Leclerc, 2008), which has been attributed to intra-bundle (tow or roving) micro-void formation. The opacity of the carbon reinforcements used in this study prevent adequate characterization of any bubbles caught inside the tows. This can be seen in Figure 3-5D and Figure 4-1A, in which the dark areas when a tow presses up against the PMMA tool prevents any discernment of bubbles (which are also dark) therein. Thus any increase in intra-tow void formation at higher velocities is most likely impossible to characterize for carbon reinforcements via the measurement methods employed in this study. Yet most failure- and damage-prediction studies of composite materials focus on the larger, inter-tow bubbles more than the intra-tow micro-bubbles, as the former seem to have a much more significant effect (Sisodia, 2015; Lambert, 2012).

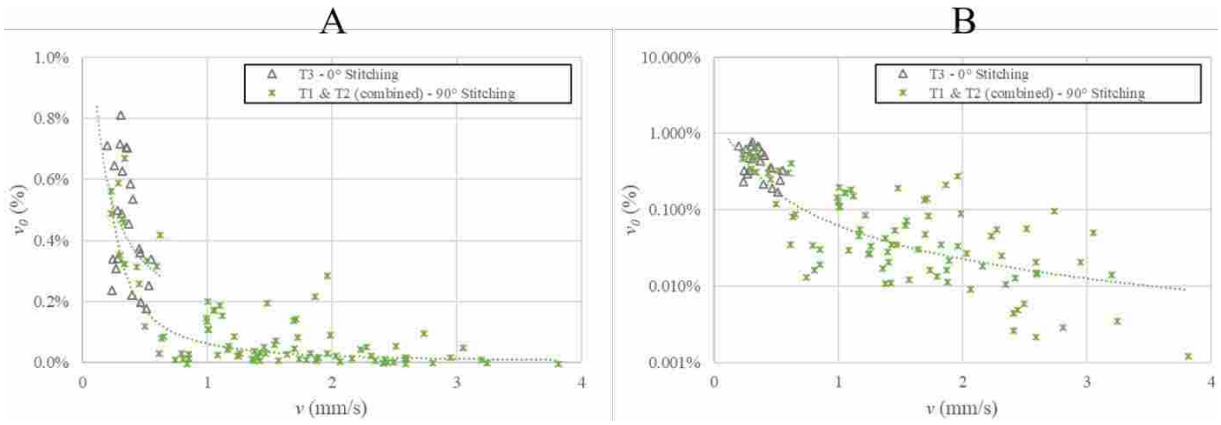

Figure 4-13: Void Concentration as a Function of Flow Front Velocity, $v_0(v)$

As can be seen in Figure 4-13 and Table 4-3, the data sets from both 90° infusions (T1 and T2) were combined and considered as a fourth group (as shown in Figure 4-13). All the data points from the 90° and 0° tests were considered collectively as a fifth group. A log-log transformation was applied to the data and a regression analysis performed for all five groupings.

The power law fits for 0° and 90° flow are 0.173 and 0.415, respectively. The low value of R^2 for the 0° infusion (T3) suggests that the curve fit to the data is not representative of any trends. It could be that this was at least partially influenced by the smaller sample size (fewer images in the image sequence analyzed) for T3, compared to the other two infusions. Of the three infusions analyzed, the *v* data for T3 showed the smallest standard deviation and spread (again, possibly due to the smaller sample size). The P-value is also relatively high, compared to the other two infusions, and would be close enough to the significant/insignificant limit to warrant further investigation, assuming a significance level of 0.05 was considered. Table 4-4 and Table 4-5 list some basic descriptive statistics regarding velocity and void content for the five data groups analyzed with regard to $v_0(v)$.

Table 4-3: Comparison of Power Law Fits for $v_0(v)$ Data

Test	*Best Fit Equation*	*R^2 Value*	*P-value*
T1	$y = 4.22E\text{-}04x^{-1.69}$	0.525	1.25E-08
T2	$y = 1.89E\text{-}03x^{-2.66}$	0.497	6.49E-08
T3	$y = 2.09E\text{-}03x^{-6.48E\text{-}01}$	0.173	4.86E-02
T1 & T2 (combined)	$y = 6.24E\text{-}04x^{-1.46}$	0.415	5.49E-12
ALL (T1, T2, & T3 combined)	$y = 6.63E\text{-}04x^{-1.54}$	0.580	8.08E-23

Table 4-4: Descriptive Statistics Regarding Flow Front Velocity v (mm/s), for the Data Groups Analyzed with Regard to $v_0(v)$

	T1	*T2*	*T3*	*T1 & T2*	*ALL*
Mean	1.03	1.99	0.35	1.51	1.27
Standard Error	0.09	0.11	0.02	0.09	0.08
Median	0.96	1.95	0.34	1.41	1.16
Standard Deviation	0.58	0.72	0.10	0.81	0.86
Sample Variance	0.34	0.52	0.01	0.66	0.75
Skewness	0.32	0.25	0.41	0.39	0.59
Range	2.11	2.82	0.35	3.58	3.61
Minimum	0.22	0.98	0.19	0.22	0.19
Maximum	2.33	3.80	0.54	3.80	3.80
Count	46	45	23	91	114

Table 4-5: Descriptive Statistics Regarding Measured Void Concentration v_0 (%), for the Data Groups Analyzed with Regard to $v_0(v)$

	T1	*T2*	*T3*	*T1 & T2*	*ALL*
Mean	0.1472%	0.0763%	0.4674%	0.1121%	0.1838%
Standard Error	0.0285%	0.0112%	0.0407%	0.0158%	0.0201%
Median	0.0364%	0.0528%	0.4604%	0.0366%	0.0805%
Standard Deviation	0.1935%	0.0753%	0.1954%	0.1508%	0.2146%
Sample Variance	0.0004%	0.0001%	0.0004%	0.0002%	0.0005%
Skewness	1.35	0.94	0.19	1.94	1.26
Range	0.6735%	0.2886%	0.6349%	0.6735%	0.8158%
Minimum	0.0002%	0.0013%	0.1811%	0.0002%	0.0002%
Maximum	0.6737%	0.2898%	0.8160%	0.6737%	0.8160%
Count	46	45	23	91	114

Stitch direction is a minor change in reinforcement architecture (keeping the same principle reinforcement fiber direction of +/- 45°), yet qualitative analysis showed significantly different mechanisms in bubble mobility after formation for the different stitch orientations. This should affect the measured void content to some extent. Regardless, despite different injection flowrates (Q) and different mobility due to stitching orientations, the initial plot of $v_0(v)$ visually

appeared to exhibit the same relationship for all infusions done with the same fiber reinforcement orientation (+/- 45°) as some of the scatter in the different datasets overlaps. The R^2 value for the power law curve for the "ALL" dataset (T1, T2, & T3 combined) at least warrants the idea that a curve fit via a power law shouldn't necessarily be rejected when comparing infusions of dissimilar stitch directions. The spread in *v0* for the combined 90° infusions data was comparable to the 0° infusion (~0.63% and ~0.67%, respectively). It is interesting to note that of the data groupings shown in Table 4-3 the value of R^2 was highest for the curve fit to all the infusion data collectively ("ALL" grouping, R^2 value of 0.580). This curve is displayed in Figure 4-14 (note the different infusion datasets are shown with different symbols, for reference). The power law fit shown in red is for the "ALL" combined dataset of 0° and 90° infusions data. Despite the differences in preform configuration (stitch orientation with respect to flow) and injection flowrates, bubbles seem to form in a similar fashion for all 3 of the NCF infusions. The images support this; the 45° flow relative to the carbon fiber tows forms bubbles against the stitch lines, regardless of stitch orientation at 0° or 90°. Bubble mobility mechanisms such as escape and entrapment are different, but the formation is similar.

An obvious limitation of this analysis of course is that only two infusions are done at 90° and one at 0°. A total sample set of three infusions does not impart high confidence in these comparisons, but this is the first known experimental comparison in void formation between different flow orientations (i.e. stitching orientations) of the same reinforcement. Future work will expand upon these infusions to attempt to further validate this comparison.

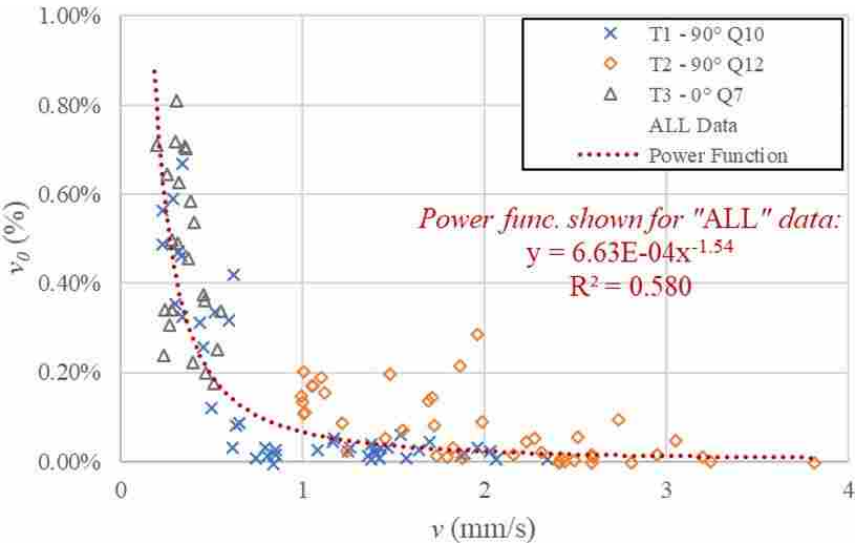

Figure 4-14: Power Law Fit for Combined 0° and 90° *v0*(*v*) Data

4.2.4 Delineation of Void Formation and Void Mobility

The *y*-axis in Figure 4-13 is not necessarily a void formation rate, but the measured void concentration in a given image's RIA. To interpret this as void formation rate at the flow front requires the assumption that all of the bubbles detected in each image were not formed outside of that particular image's RIA, i.e. previously during the infusion. Bubble mobility (Frishfelds, 2008) may cause some of the bubbles, formed earlier in the infusion, to eventually slip out of the spot in which they were formed and be moving towards the flow front when captured in a photograph at a later infusion time, a phenomenon that was observed first-hand during this study.

In an attempt to distinguish between bubbles formed in a given image's RIA and those that move moved into the RIA from previous formation locations, the number of stationary bubbles vs. mobile bubbles was quantified by comparing the analysis for RIA lengths of 20 mm and 60 mm. This is related to the RIA length choices shown in Figure 3-8, and the comparison made in Figure 4-5. The instantaneous flow front velocity was variable over the 40 mm length between

these two RIA ends, thus void formation should also be different. But that difference in v across a 40 mm length is not as large as a constant pressure infusion, and the difference was small for the first 80 mm and the latter half of the infusion, from 150 to 300 mm (Figure 4-8). Thus void formation rates can be assumed to be fairly constant across those regions. If the void formation rate is assumed to be constant, then if the bubbles remain completely unchanged after formation, e.g. remaining where they were formed and no change in size, the void content measured in RIA's with 20 and 60 mm should be equal, recalling that v_0 is measured as the percentage of voids in an area. However, some shrinkage occurs due to the rising pressure gradient, which would affect v_0 for the 60 mm RIA more than the 20 mm RIA, as the former includes bubbles closer to the high pressure inlet area. To illustrate the shrinkage expected to occur, a small sample of static bubbles was selected from T3 (as it showed the highest average v_0 of the NCF infusions, see Table 4-5). When using rigid RTM tooling (as was done in this study) the pressure at a given length from the inlet (x), between the inlet and flow front, is a linear equation:

$$P(x) = (P_{vent} - P_{inlet})\frac{x}{L} + P_{inlet} \tag{4-3}$$

The flow front position was correlated with the pressure sensor data described earlier to thus calculate the expected pressure at a given bubble's observed position. The cross-sectional area was measured in multiple images for two sample bubbles from T3. These bubbles were static (stuck in place). The results of this are illustrated in Figure 4-15, which show the expected linear trend of reduction in bubble cross-sectional area with increased distance between the bubble position and the flow front. Figure 4-15A shows cross-sectional area as a function of distance from the flow front; Figure 4-15B shows area as a function of the calculated pressure for a bubble's position (relative to flow front).

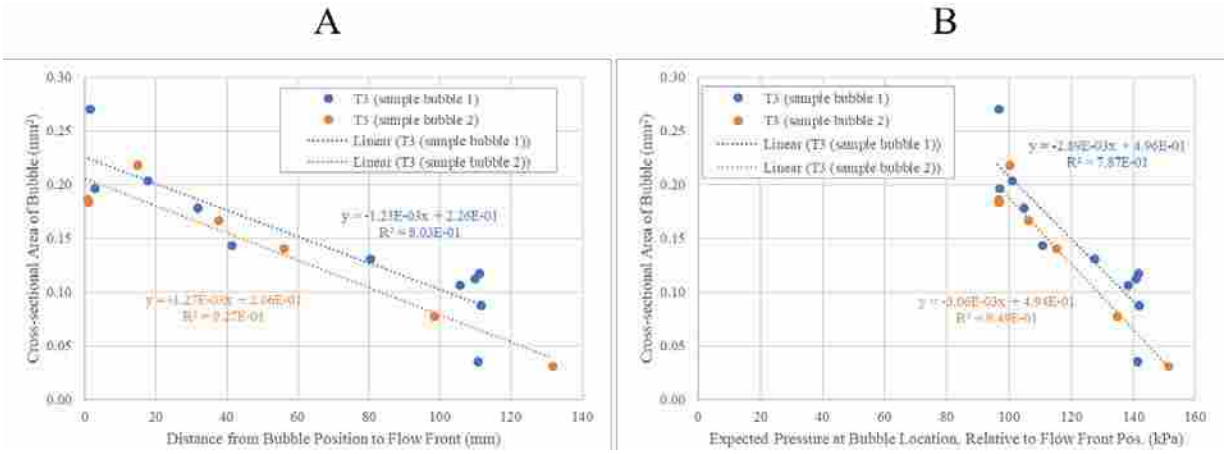

Figure 4-15: Cross-sectional Area of Static Bubbles as a Function of Distance from Flow Front

Some bubbles do escape their place of formation, moving towards the flow front, and escaping to the air on the downstream side of the flow front (removing voids from the infusion). The percentage of bubbles which escape thus through the flow front should be reflected by a lower v_0 in the 60 mm RIA, as the chance that a bubble escapes is greater towards the high-pressure inlet side of the mold.

Figure 4-16 shows a plot of $v_0(L)$ for all T1, T2, and T3 data for both 20 mm and 60 mm RIA lengths (measured from the trailing flow front position). Although not a clear relationship, there is often a slight reduction in v_0 when considering the 60 mm RIA. The ratio of the measured v_0 for the 20 mm long RIA to the 60 mm long RIA was then calculated and again plotted against v in Figure 4-17. When evaluating all three tests simultaneously, a rough increasing relationship can be seen, implying that increasing the flow front velocity results in a larger difference in bubble volume between the 20 mm long and 60 mm long RIAs. This is intuitive, as a higher velocity would be caused by a higher pressure gradient, which in turn would cause more bubble dissipation (i.e. shrinkage, dissolution, and mobility) over a given length in the filled regime.

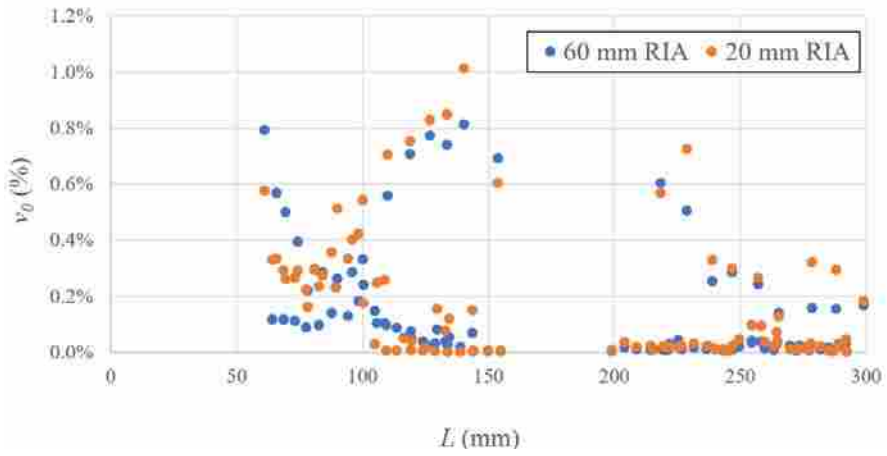

Figure 4-16: Comparison of $v_0(L)$ for RIA Lengths of 20 and 60 mm

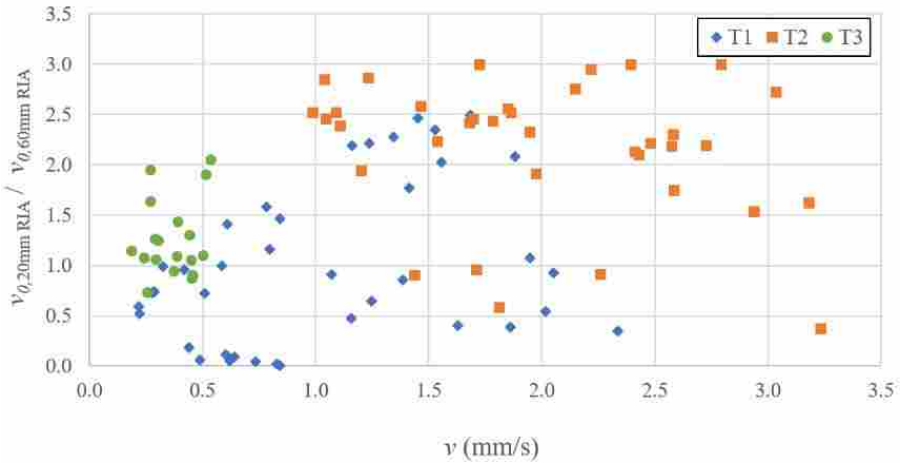

Figure 4-17: Ratio of v_0 for 20 mm vs. 60 mm RIA, as a Function of Front Velocity

A brief bubble velocity study was conducted to empirically support the idea that bubbles trapped farther upstream will migrate at higher velocities than bubbles which begin to migrate while still close to the flow front. In this context bubble migration was taken to mean mobility, i.e. a bubble's change in position within the preform architecture. For the macro-voids observed in this study, this most-often occurred along the inter-tow channels or spaces.

A frame-by-frame analysis of T1, T2, and T3 was performed to identify a sample set of individual bubbles that migrated post-formation. The pre- and post-migration locations for these bubbles were calculated (relative to the preform start, L=0, and the trailing edge of the flow front) by tracking the position(s) of each bubble in a sequential series of images (between 2 and 4 total frames per bubble, dependent on the bubble's visibility). Positions referenced the approximate centroid of each bubble's visible area. Whenever possible, the bubbles studied were selected from within the centered 50% of the preform width (similar to what was done for the RIAs defined within MATLAB).

A simple calculation for migratory velocity (i.e. velocity along the direction of travel) was made using the calculated change in position and the known time interval between image captures. Each bubble's velocity was then plotted against the distance of its pre-migration position from the flow front (measured normal from the flow front's trailing edge upstream to the bubble). The results are shown in Figure 4-18. Though a small sample set, it was observed that bubbles which had pre-migration positions farther upstream generally migrated at higher velocities than the bubbles with pre-migration positions still in close proximity to the flow front. Though there is overlap in the scatter of each test's data, it appears that T2 had the higher general bubble velocities for a given distance from the flow front, followed by T1 and then T3. This agrees with the hierarchy of different Q values used during injection of each test, as T2 had the highest specified injection flow rate on the RTM machine, followed by T1 and then T3. Power law fits are shown with Figure 4-18, though it should be noted that T2 is included for comparison only as it does not represent a strong fit compared to the fits made to the other two data sets.

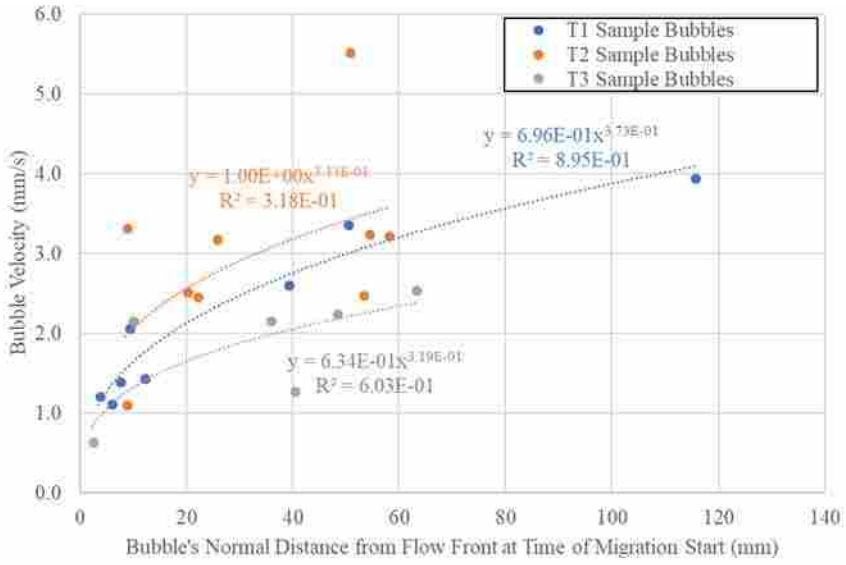

Figure 4-18: Bubble Migration Velocity as a Function of Pre-migration Distance from the Flow Front

To investigate the possible effect of stitching orientation on these formation-migration relationships, an analysis of bubble mobility was made by observing post-formation bubble behavior in a set of sampled image sequences. The key findings from this analysis are first summarized here, and then detailed figures and further discussion for each image sequence analyzed is presented.

It was observed that when stitching was oriented at 90° (perpendicular to the principle flow direction) roughly 50% of the bubbles formed at the flow front began to migrate right away, though they would get stuck intermittently by subsequent stitches as they moved downstream. The other 50% of bubbles formed at the front remained stuck where formed for a short time but were observed eventually moving downstream (not dissipating in place). In contrast, it was observed that when stitching was oriented at 0° (parallel to the flow direction) the overall bubble content appeared higher, on average. Of the static bubbles formed at the flow front roughly 26%

moved from their formation location right away but then became stuck mid-migration, compared to roughly 62% of the static bubbles formed at the front which remained immobile, stuck where they were initially formed until finally shrinking and dissipating from the increasing fluid pressure.

The first image sequence analyzed was from one of the 90° infusions (T2). These image samples and their bubble count data are shown in Figure 4-19 and Table 4-6, respectively. The area within the images sampled was a small, static location near the inlet and roughly within the center of the preform width. The progressive images show that when the stitching was oriented at 90° roughly 25% of the original discreet voids formed at the flow front were rendered immobile immediately upon their formation. These "stuck-where-formed" bubbles exhibited no initial migration and remained in place at their formation site. The formation site was typically adjacent the stitch fibers, though sometimes it was within the small stitch loop architecture itself (i.e. an "intra-stitch void", as was the case of the smallest stationary bubble seen near the bottom edge of Image 2 in Figure 4-19). Other bubbles became immobile when, during initial post-formation migration along an inter-tow channel, they encountered a stitching row and subsequently got stuck. For the non-moving bubbles observed in Figure 4-19 it appears that this "halted migration" scenario applied to roughly 55% of the total original number of discreet bubbles formed at the flow front ($t = 0$) and was thus more common than the "stuck-where-formed" behavior described above. After roughly 1 minute all non-moving bubbles in the image sample had either moved or dissipated.

Discussion of Figure 4-19 has thus far considered comparisons of void concentration with the total original number of discreet bubbles formed at the flow front for the given image set. In

practice it is likely better for flow visualization studies to describe the migration history of the bubbles visible at any given time. Thus an additional interpretation of the data in Table 4-6 is

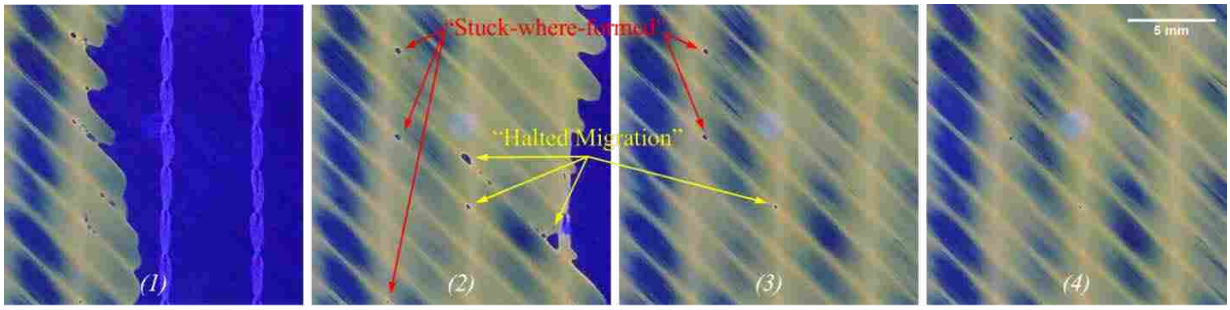

Figure 4-19: Images Analyzed for 90° Stitching Bubble Entrapment Study

Table 4-6: Study of Initial Bubble Entrapment with 90° Stitching

Test	*Stitch Orientation*	*Image #*	*Time (s)*	*QTY, Discreet Bubbles Visible in Image (total)*	*Non-moving Bubbles*	
					QTY, "halted migration"	*QTY, "stuck-where-formed"*
T2	90°	1	0	13	-	-
T2	90°	2	+8	10	7	3
T2	90°	3	+22	4	2	2
T2	90°	4	+48	2	1	1
T2	90°	-	(+62)	(0)	-	-

that on average roughly 50% of the discreet bubbles visible at any given time are "stuck-where-formed", and 50% are those that had previously been moving but then became stuck ("halted migration"). Obviously there will also be bubbles captured in images which are actively migrating, but it was observed that such migratory bubbles in the 90° test infusions in this study were typically exhibiting the stop-start behavior mentioned earlier (see section 4.1) and would be seen as bubbles stuck with halted migration because they were not exhibiting active, free

mobility when captured in a given image/image sequence. Similar analysis of a near-inlet area for images from T3 (stitch in the 0° direction) showed that migration behavior was closely related to the orientation of the stitching versus the reinforcement fibers (which were oriented at 45°) with respect to flow. Results of these bubble entrapment observations are presented in Figure 4-20 and Table 4-7. Note that for each sample image the cumulative total number of discreet voids visible is considered, not just those seen being formed in Image 1.

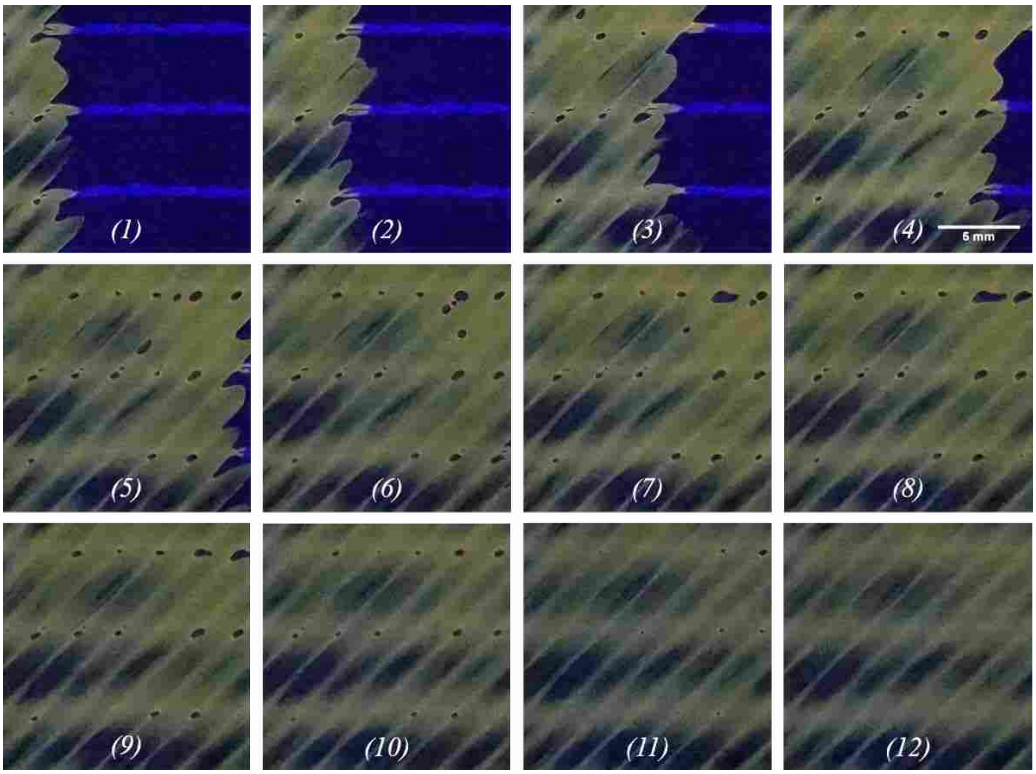

Figure 4-20: Images Analyzed for 0° Stitching Bubble Entrapment Study

With stitching at 0° a clear majority of the bubbles formed at the front remained stuck in their initial locations. In the sample images in Figure 4-20 an average of 62% of the bubbles visible at any given time are “stuck-where-formed”, while only 26% of the bubbles shown at any given time are those categorized as “halted migration” (the remaining bubbles in the image are those

seen to be actively migrating). Thus bubble migration was less present with the stitching oriented at 0° (compared to 90°), though an instance of it was observed occurring along both inter-tow channels and stitch paths at the top of Images 5 - 8. When bubbles migrated along either of these paths there was high probability they would encounter another bubble and have opportunity to merge together. These new, larger bubbles would often begin to elongate along the stitch (not the tow channel) in the direction of the flow front.

Table 4-7: Study of Initial Bubble Entrapment with 0° Stitching

Test	*Stitch Orientation*	*Image #*	*Time (s)*	*QTY, Discreet Bubbles Visible (total)*	*Non-moving Bubbles*	
					QTY, "halted migration"	*QTY, "stuck-where-formed"*
T3	0°	1	0	5	-	-
T3	0°	2	+6	7	-	4
T3	0°	3	+16	11	-	4
T3	0°	4	+28	14	-	9
T3	0°	5	+32	17	2	11
T3	0°	6	+36	18	3	13
T3	0°	7	+42	18	3	12
T3	0°	8	+54	16	5	11
T3	0°	9	+74	17	6	11
T3	0°	10	+294	14	5	9
T3	0°	11	+534	9	3	6
T3	0°	12	+774	0	-	-

When bubbles split, part of the parent bubble would remain in place while the rest (now a new, discreet bubble) would continue migrating until it met with another bubble or the flow front. This was shown to be true even if the parent bubble was already small before splitting, and/or if there was no interaction with another bubble immediately prior to the split event.

These migration behaviors related to 0° stitching orientation are further illustrated in another series of progressive images from T3, shown in Figure 4-21. (Note that Image 1 in Figure 4-21 is a detailed view of the top center portion of Image 8 in Figure 4-20.) Images (1 to 6) show time at t=0 s, +120 s, +194 s, +201 s, +205 s, and +207 s, respectively. A bubble which has shown to remain stuck for a significant span of time suddenly splits (Figure 4-21 Image 3), leaving behind a small remainder as the majority of the bubble then travels along the inter-tow channel to the next stitch area (Image 4). This type of split-then-migrate behavior appears to

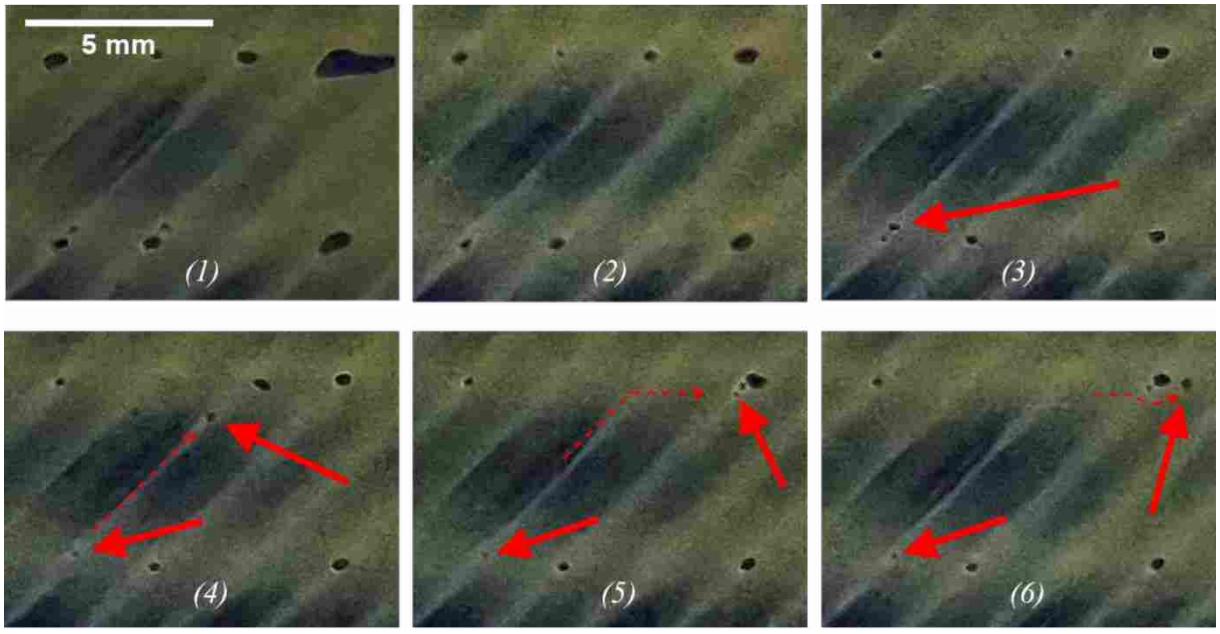

Figure 4-21: Bubble Migrations Along Tow Channel and Stitch Channel Paths

initiate migration of other small bubbles, and seems to allow for changes of migration path (stitch vs. tow channel; Images 5 and 6). It was observed that if a bubble did not migrate shortly after being formed, or if it did not merge with another bubble and become larger, then it was very likely that it would remain stuck in place, even with the rising resin pressure at that location as the flow front moved downstream.

With the stitch oriented at 0°, larger bubbles were formed in the tow channel adjacent to the stitching fibers when local fluid saturation along the length of a tow met with a partially-saturated stitching fiber. Figure 4-22 illustrates an example of this observed formation mechanism for the given fiber architecture in T3 (0° stitch orientation) by following the formation location of a bubble, and then the bubble itself, through progressive images.

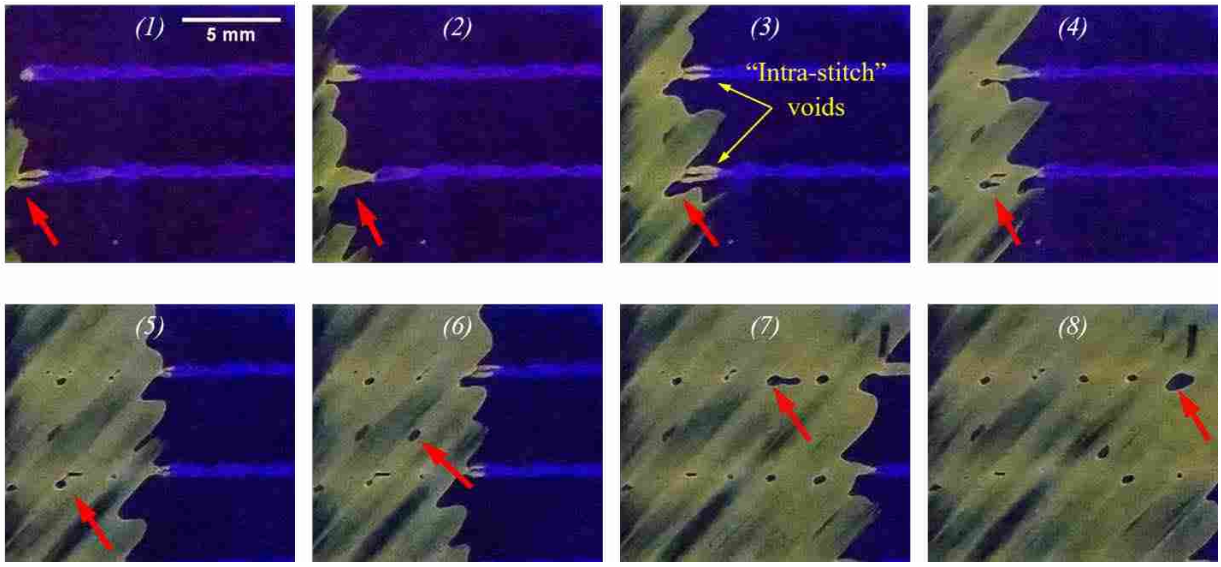

Figure 4-22: Local Fluid Saturation Along Tow Meets with a Partially-Saturated Stitch Fiber

The progress of an individual bubble is indicated by the red arrow in each image. Bubble progress is shown at time (t) of 0 s, +4 s, +10 s, +12 s, +18 s, +20 s, +32 s, and +40 s. Smaller bubbles were formed within the loops of the chain-stitch architecture where capillary action wets the stitch thread, encircling a portion of dry reinforcement fibers (Image 3 in Figure 4-22). This latter scenario was less likely to produce a bubble, and these "intra-stitch" bubbles were small enough that they typically disappeared within a few frames in the photograph sequence (a few seconds).

In general, the bubble formation observed in the T2 and T3 images seems to support the literature which addresses bubble formation in LCM as a function of saturation time scale differences for filling of intra- and inter-tow pores (Park, 2011; Labat, 2001). Even though all *in situ* bubbles observed in this study were macro-voids the principle still applies: different fiber materials and geometries within a textile will exhibit different saturation time scales, causing mechanical entrapment of bubbles.

Previous literature has presented models for movement of bubbles in such NCF fabrics (Frishfelds, 2008). These models incorporate predictions of when a bubble will escape from its place of entrapment, and the chances of splitting, merging with other bubbles, changing paths, and becoming entrapped again. Little experimental evidence of this behavior has been seen, however, until now afforded by the *in situ* photographs in this study. The bubble focused on in Figure 4-22 shows complete formation by Image 4 and stays stuck in place against the underside of the stitching fiber where it was formed for at least 2 subsequent images. In Image 6, the bubble splits, leaving a small bubble at the stitch while the rest manages to migrate across the stitch and continue down the inter-tow channel. In Image 7, the bubble reaches the next stitch line and becomes entrapped again, merging with another bubble just formed at that same location. Some of the bubble again manages to split away from the entrapped bubble, but instead of continuing along the inter-tow channel, it veers to the right and follows the stitch line, merging with two other bubbles along the path, ending up as a large combined bubble, stuck at an intersection between stitches and inter-tow gaps (Image 8).

The effect of the 0° (versus 90°) stitch can be seen in how bubbles migrate from their initial formation location. For 90° flow (T1 and T2), the bubbles follow inter-tow gaps until hitting a stitch line which acts as a barrier, but the bubbles do not change their course. Once

crossing the stitch line, they continue in their previous path, along the same inter-tow gap. In contrast, for 0° flow (T3, Figure 4-21 and Figure 4-22) it appears that most of the bubbles formed by the flow front will often remain in place (i.e. "stuck-where-formed") for longer periods – sometimes indefinitely (or until dissolved into solution by the increasing resin pressure). Two general patterns of movement were observed for bubbles that did begin to migrate. First, once the migrating bubbles reach a new stitch line it is possible for their flow path to switch from the inter-tow channel to the stitch line itself. Such path switching behavior was only exhibited in a small minority of the void migration events sampled. It is likely due to a flow channel being caused by the stitch threads locally compressing the fabric away from the tooling, and the shorter path to the low pressure flow front when moving parallel to the 0° flow direction along the stitch fiber. As discussed below, however, bubbles did not seem to truly reach the front by traveling along stitch channels in the warp direction, they would almost always make final migration to the front via a tow channel path. Of note is that bubbles do not travel on top or through the stitching geometry, instead they move along that side of the stitch which they first encounter (Images 7 and 8 in Figure 4-22). This increased the likelihood for bubble-to-bubble interaction, with many colliding bubbles combining and subsequently splitting later in the migration.

A second pattern observed was that there was higher likelihood for the bubbles migrating near the flow front to travel along the inter-tow-channels (i.e. principle fiber direction, in the case of T3, 45°) instead of the 0° direction along the stitch fiber (i.e. directly toward the vent). This seemed to apply without regard for previous migration behavior. This behavior concentrates the bubbles on the top surface of the sample in the direction of the fibers, i.e. towards the top of the images in Figure 4-22. It is assumed that this same type of bubble movement is occurring along

the fibers in the other layers through the thickness of the sample. As there are a balanced number of layers in both the +45° and -45° directions, this would concentrate the bubbles on either side of the flow direction, with less bubbles down the middle.

Figure 4-23 illustrates the difference in distribution of bubble concentration over time. Image samples of equal size were taken from the same *L* position in the preform, approximately

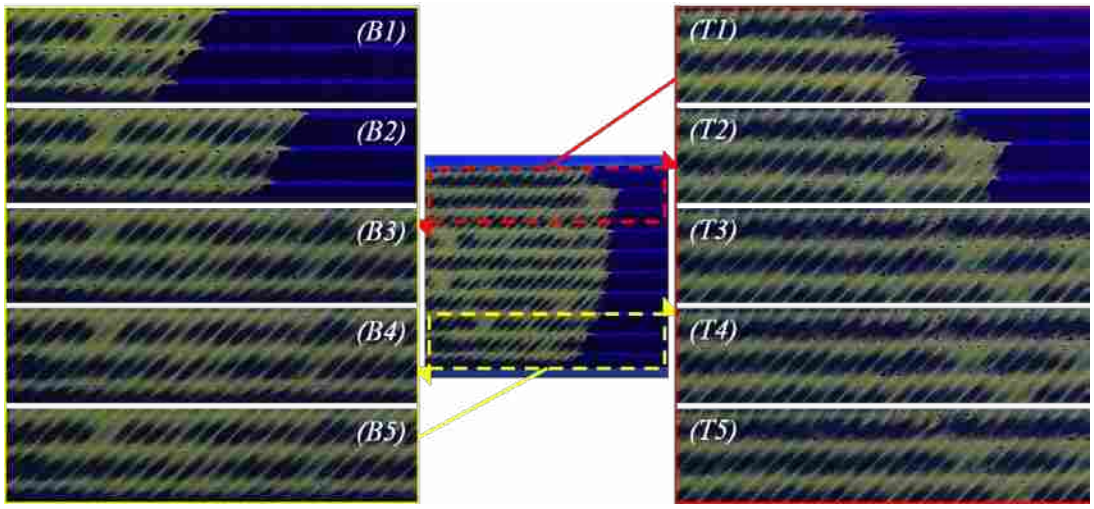

Figure 4-23: Bubble Accumulation Over Time, for Locations Near Preform Edges

Table 4-8: Bubble Accumulation Study for Selected T3 Images

Test	*Stitch Orientation*	*Image Pair #*	*Time (s)*	*v_0 %, Top Edge (T)*	*v_0 %, Bottom Edge (B)*
T3	0°	1	0	0.269	0.544
T3	0°	2	+17	0.733	0.445
T3	0°	3	+56	1.090	0.205
T3	0°	4	+67	1.044	0.216
T3	0°	5	+122	0.829	0.047

180 mm from the inlet, at both the top and bottom edge area of the preform width. Image pairs in the figure are numbered progressively, beginning with 1 for the earliest image; the top and

bottom images are noted with T and B, respectively. Each top/bottom image pair was taken from the same source image, as shown in the center illustration of Figure 4-23. Note that these areas are outside of the center preform area considered in the RIA analysis described in the previous sections. V_0 was calculated for the top and bottom images. This was done for 5 separate top/bottom pairs at progressively later times to investigate dynamic bubble mobility. The results of this study are shown in Table 4-8. Note that after approximately 2 minutes the bubble volume at the top edge (the leading down-stream tow position) is over 10x higher than the bubble volume observed at the bottom edge.

4.2.5 Correlation of Void Content to Flow Front Lag

The void formation models related to dual-scale flow (i.e. difference in flow velocity between intra-tow and inter-tow, or the stitches) predict that the minimal void formation is caused by equal flow front velocities in all regions of the reinforcement. Correspondingly, the degree of void formation should correlate positively with the magnitude of the difference between the leading and trailing edges of the flow front. This difference can be seen in Figure 4-22 where the flow seems to "finger" through the middle of the carbon tows and lag in the inter-tow channels. This is the predicted environment for slow bulk flow and corresponding macro-bubble formation within the inter-tow gaps. The difference in position between the leading and trailing edges, termed lag, is illustrated in Figure 4-24. Here the leading and trailing edge locations are marked with pink and yellow lines, respectively. Dashed lines represent the RIA width boundary. The lag distance (approx. ~ 8 mm for the image shown in the figure) is noted with red arrows. Using this method, and with the flow front position data from MATLAB, the approximate flow front lag was calculated for several images from throughout the entire infusion duration for T1, T2, and T3. Figure 4-25 shows v_0 as a function of the lag length data results.

Interestingly, the trend is the opposite of what would be expected; images with longer lag gap exhibit less visible void content. The cause for this is unknown but may have something to do with differences in mobility, i.e. more voids may form at higher lag lengths, but move or shrink by pressure faster given the process environment that creates the larger lags. A higher v_0 in the 0° infusion (T3), compared to perpendicular flow (T1 and T2), is observed when considering the same lag length value.

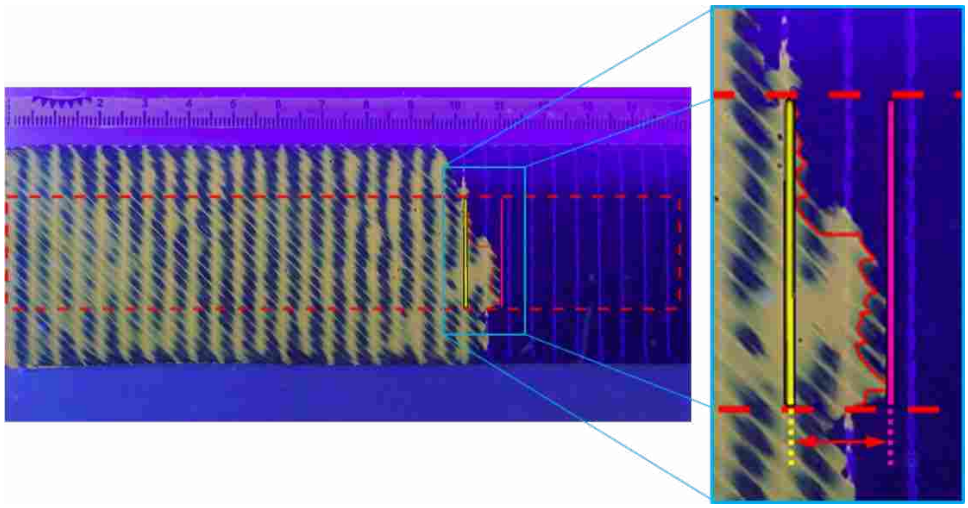

Figure 4-24: Illustration of Lag Distance Between Leading and Trailing Edges

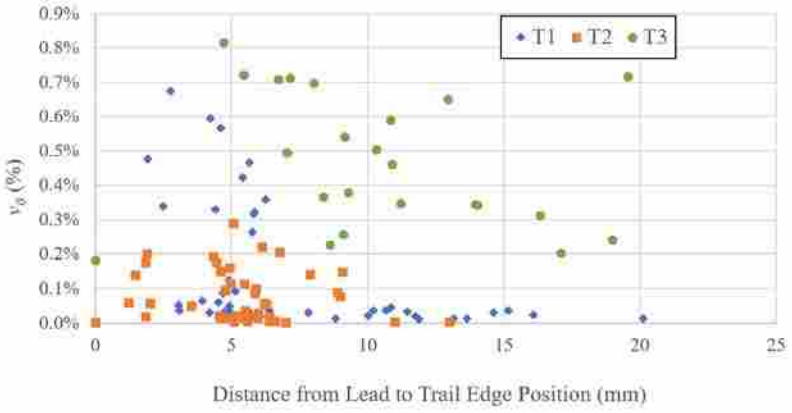

Figure 4-25: v_0 as a Function of Flow Front Lag Length

4.2.6 MATLAB Results

The work of this study included developing a MATLAB analysis strategy for use in batch processing sequential image sets. The semi-automated measurement methods employed in MATLAB allowed for objective collection of large data batches from multi-image sequences. As outlined in the methodology, the multi-step process used to configure the relevant settings for a given image sequence proved useful in reducing overall time required to convert multiple images into binary form for subsequent bubble measurements. Despite the present work's inability to produce acceptable batch image sequence data for the infusions done with Oxeon STW fabric, the use of MATLAB to process and analyze binary images of NCF for void content has garnered satisfactory results. For the images analyzed in this study it was found that best results were obtained by color segmenting an RGB image, then thresholding only the red and green channels to produce two binary images, and then subsequently combining the two to form a composited binary image. It was found that excluding the blue channel from consideration yielded maximum detail and better (if not equal) accuracy in the final binary image. Any excess areas or pixel noise could then be filtered out per the aforementioned software methodology, which included semi-autonomous filtering with pre-defined settings for allowed pixel regions, as well as the option to remove or add user-specified regions. The strategy of overlaying each binary image onto the original source photo as a final double check of results and opportunity for manual removal or addition of pixel areas proved very effective, increasing the accuracy of subsequent data from binary results with only minimal increases to user-induced subjectivity and total analysis time per image.

The results of this work have shown that analysis of progressive image sequences can greatly enrich the volume of *in situ* measurements for a given study without compromising the

data quality. Other recent resin flow studies agree that MATLAB has shown to be a powerful tool for image-based *in situ* flow analysis (Causse, 2018).

4.3 Future Recommendations

It is recommended that future work be done to further-validate the results of this study by producing cured laminates by a similar methodology and then correlating observed final void contents with *in situ* void formation data. Understanding the relationship between *in situ* void formation, pre-cure bubble behavior, and cured-in-place void results will directly support future research in both predictive void formation modeling and LCM process development.

For future iterations of similar work, it is advised that consideration be given to camera and image capturing parameters. The use of two static cameras in this study contributed many advantages to obtaining clear, consistent images of the entire preform sample area. The space required by the dual camera setup influenced how close to the mold the cameras could be placed, reducing the overall pixels-per-millimeter ratio and thus the overall resolution possible (1 pixel of area measured roughly 710 μm^2). The work of this study focused primarily on characterizing flow front formation (and subsequent migration) behavior of macro-voids and was able to obtain satisfactory results with the presented image capture methodology, but it is likely that future work regarding *in situ* flow analysis, especially that which is focused on micro-bubble flow or tow saturation, would greatly benefit from higher resolution images.

There is potential to further-develop the software strategy for sequential image analysis to be more accurate when locating the flow front location for a given image. This was highlighted in the recent efforts of Causse et al. (Causse, 2018), which showed that implementation of more-accurate software tools will enable better semi-automated measurement results. This also applies

to implementing additional data tools aimed at characterizing the bubbles being formed at the flow front in more detail, tracking their migration, and so on. Such work will support the continuing efforts of finding new relationships and developing subsequent metrics to then measure for predicting v_0 as a function of observable flow front characteristics.

5 CONCLUSIONS

The purpose of this research is to empirically investigate flow front void formation rates and post-formation bubble mobility behavior for composites produced via resin transfer molding (RTM). While there have been several recent papers discussing theoretical models to predict void formation and bubble mobility, little literature exists on empirical, in situ analysis of void formation rate(s) during liquid composite molding processes.

In situ observation of infusions was accomplished by photographing resin flow progression during the infusion phase of each test. Published models for movement of bubbles incorporate predictions of when a bubble will escape from its place of entrapment, and the chances of splitting, merging with other bubbles, changing paths, and becoming entrapped again. Little experimental evidence of this behavior has been seen, however, until now afforded by the *in situ* photographs and data presented in this study.

The work of this study included developing a MATLAB analysis strategy for use in batch processing sequential image sets, which employed the representative image area (RIA) method to evaluate v_0. It was found that the shorter the RIA length, and the more it follows the true flow front shape, the more representative the measured v_0 was of the void formation at the flow front. The use of MATLAB to process and analyze binary images of infusions for void content has garnered satisfactory results. The employed semi-automated measurement methods allowed for objective collection of large data batches from multi-image sequences. and has shown that

analysis of progressive image sequences can greatly enrich the volume of *in situ* measurements for a given study without compromising the data quality.

Void formation is presented as a function of flow front velocity. Despite the differences in preform configurations (stitch orientation with respect to flow) and injection flowrates, bubbles seemed to form in a similar fashion for the 3 infusions of carbon fiber NCF reinforcement analyzed in this study. The images support this; the 45° flow relative to the carbon fiber tows forms bubbles against the stitch lines, regardless of stitch orientation at 0° or 90°. Bubble mobility mechanisms (such as escape and entrapment) were observed to be different for dissimilar configurations, but formation at the front appears to be similar.

The void formation models related to dual-scale flow (i.e. difference in flow velocity between intra-tow and inter-tow, or the stitches) predict that the minimal void formation is caused by equal flow front velocities in all regions of the reinforcement. Correspondingly, the degree of void formation should correlate positively with the magnitude of the difference between the leading and trailing edges of the flow front. Interestingly, the trend observed in this study is the opposite of what would be expected; a longer gap between leading and trailing flow front edges results in lower observed void content. The cause for this is unknown but may have something to do with differences in mobility, i.e. more voids may form at higher lag lengths, but move or shrink faster by pressure given the process environment that creates the larger lags.

Bubble migration is documented for infusion of NCF reinforcement with stitching and fiber tows at different orientations. When stitches and tows are oriented at 0° (warp) and 45°, respectively, migration can be seen occurring along both inter-tow channels and stitch paths. If a bubble did not migrate shortly after being formed, or if it did not merge with another bubble and become larger, then it was very likely that it would remain stuck in place, even with the rising

resin pressure as the flow front moved downstream. When stitches and tows are oriented at 90° (weft) and 45°, respectively, it is observed that bubbles follow inter-tow gaps until hitting a stitch line (which acts as a barrier). Once crossing the stitch line they resume migrating along the same inter-tow gap toward the flow front.

It was observed that when stitching was oriented at 90° (perpendicular to the principle flow direction) roughly 50% of the bubbles formed at the flow front began to migrate right away, though they would get stuck intermittently by subsequent stitches as they moved downstream. The other 50% of bubbles formed at the front remained stuck where formed for a short time but were observed eventually moving downstream (not dissipating in place). In contrast, it was observed that when stitching was oriented at 0° (parallel to the flow direction) the overall bubble content appeared higher, on average. Of the static bubbles formed at the flow front roughly 26% moved from their formation location right away but then became stuck mid-migration, compared to roughly 62% of the static bubbles formed at the front which remained immobile, stuck where they were initially formed until finally shrinking and dissipating from the increasing fluid pressure.

The present work was unable to produce acceptable batch image sequence data for the infusions done with Oxeon STW reinforcement due to the complex, small-scale details captured in the images of this fabric. Though no v_0 results are presented for this reinforcement, a frame-by-frame evaluation of infusion images for bubble formation and entrapment yielded some qualitative observations with regard to the effect of binder geometry. Bubbles collect and coalesce in the furthest-forward position within a given binder boundary area. In areas with more-regular binder bead geometry (i.e. geometry with smooth, continuous arcs) there appeared

to be fewer discreet bubbles present, though the size of these bubbles tended to be larger than those trapped in irregular (i.e. “messy”) binder patterns.

Recommendations are given for future studies involving image-based analysis of *in situ* bubble formation.

REFERENCES

ASTM D3171 2015.

Arcila, Iván David Patiño, et al. 2016. "Boundary element simulation of void formation in fibrous reinforcements based on the Stokes–Darcy formulation." *Computer Methods in Applied Mechanics and Engineering* 304: 265-293.

Bickerton, S., et al. 2000. "Fabric structure and mold curvature effects on preform permeability and mold filling in the RTM process. Part II. Predictions and comparisons with experiments." *Composites Part A: Applied Science and Manufacturing* 31, no. 5: 439-458.

Bickerton, S., et al. 2000. "Fabric structure and mold curvature effects on preform permeability and mold filling in the RTM process. Part I. Experiments." *Composites Part A: Applied Science and Manufacturing* 31, no. 5: 423-438.

Brandley, Mark Wesley. 2015. "Void Modeling in Resin Infusion." BYU ScholarsArchive. https://search.lib.byu.edu/byu/record/sa.etd-6459.

Breard, J., et al. 2003. "Analysis of dynamic flows through porous media. Part I: Comparison between saturated and unsaturated flows in fibrous reinforcements." *Polymer Composites*24, no. 3: 391-408.

Cann, Michael T., Daniel O. Adams, and Claudio L. Schneider. 2008. "Characterization of Fiber Volume Fraction Gradients in Composite Laminates." *Journal of Composite Materials* 42, no. 5: 447-466.

Carlsson, Leif A., Donald F. Adams, and R. Byron Pipes. 2014. *Experimental characterization of advanced composite materials*CRC press.

Causse, Philippe, Christophe Ravey, and François Trochu. 2018. *Capillary Characterization of Fibrous Reinforcement and Optimization of Injection Strategy in Resin Transfer Molding*. Vol. 2.

Celle, Pierre, Sylvain Drapier, and Jean-Michel Bergheau. 2008. *Numerical modelling of liquid infusion into fibrous media undergoing compaction*. Vol. 27. http://www.sciencedirect.com.erl.lib.byu.edu/science/article/pii/S0997753807001003.

de Almeida, Sérgio Frascino Müller and Neto, Zabulon dos Santos Nogueira. 1994. "Effect of void content on the strength of composite laminates." *Composite Structures* 28, no. 2: 139-148, http://www.sciencedirect.com/science/article/pii/0263822394900442.

Endruweit, Andreas, et al. 2011. "Mapping of the fluid distribution in impregnated reinforcement textiles using Magnetic Resonance Imaging: Application and discussion." *Composites Part A: Applied Science and Manufacturing* 42, no. 10: 1369-1379.

Frishfelds, Vilnis, T. Staffan Lundström, and Andris Jakovics. 2008. *Bubble motion through non-crimp fabrics during composites manufacturing*. Vol. 39. http://www.sciencedirect.com/science/article/pii/S1359835X07002382.

Gangloff Jr., John J., Claire Daniel, and Suresh G. Advani. 2014. "A model of two-phase resin and void flow during composites processing." *International Journal of Multiphase Flow* 65: 51-60.

Gourichon, B., C. Binetruy, and P. Krawczak. 2006. "Experimental investigation of high fiber tow count fabric unsaturation during RTM." *Composites Science and Technology* 66, no. 7-8: 976-982.

Gourichon, B., C. Binetruy, and P. Krawczak. 2006. "A new numerical procedure to predict dynamic void content in liquid composite molding." *Composites Part A: applied science and manufacturing* 37, no. 11: 1961-1969.

Gueroult, Se, et al. 2014. "Analytical modeling and in situ measurement of void formation in liquid composite molding processes." *Advanced Composite Materials* 23, no. 1: 31-42.

Guo, Zhan-Sheng, et al. 2009. "Critical void content for thermoset composite laminates." *Journal of Composite Materials* 43, no. 17: 1775-1790.

Hamidi, Youssef K., Levent Aktas, and M. Cengiz Altan. 2005. "Effect of packing on void morphology in resin transfer molded E-glass/epoxy composites." *Polymer composites* 26, no. 5: 614-627.

Hamidi, Youssef K., Levent Aktas, and M. Cengiz Altan. 2004. "Formation of Microscopic Voids in Resin Transfer Molded Composites." *Journal of Engineering Materials and Technology* 126, no. 4: 420-426.

Hoagland, David Wayne. 2017. "Continuous permeability measurement during unidirectional vacuum infusion processing.", *All Theses and Dissertations*. 6457. https://scholarsarchive.byu.edu/etd/6457.

Huang, Hansong and Ramesh Talreja. 2005. "Effects of void geometry on elastic properties of unidirectional fiber reinforced composites." *Composites Science and Technology* 65, no. 13: 1964-1981.

Hurtado, Francisco J., et al. 2015. "Numerical study of the vacuum infusion process for laminated composites with different fiber orientations." *Jnl of Reinforced Plast and Composites*34, no. 3: 196-212.

Judd, N. C. W. and W. W. Wright. 1978. "Voids and Their Effects on the Mechanical Properties of Composites, an Appraisal." *SAMPE Q* 14: 10-14.

Kang, Kai and Kurt Koelling. 2004. "Void transport in resin transfer molding." *Polymer composites* 25, no. 4: 417-432.

Kas, Y. Onur and Cevdet Kaynak. 2005. "Ultrasonic (C-scan) and microscopic evaluation of resin transfer molded epoxy composite plates." *Polymer Testing* 24, no. 1: 114-120.

Kuentzer, Nina, et al. 2006. "Permeability characterization of dual scale fibrous porous media." *Composites Part A: Applied Science and Manufacturing* 37, no. 11: 2057-2068.

Labat, Ludovic, et al. 2001. *Original use of electrical conductivity for void detection due to injection conditions of composite materials*. Vol. 329. http://www.sciencedirect.com/science/article/pii/S1620774201013630.

Lambert, J., et al. 2012. *3D damage characterisation and the role of voids in the fatigue of wind turbine blade materials*. Vol. 72. http://www.sciencedirect.com/science/article/pii/S0266353811004155.

LeBel, Francois, Edu Ruiz, and Francois Trochu. 2017. "Void content analysis and processing issues to minimize defects in liquid composite molding." *Polymer Composites*.

LeBel, Francois, et al. 2014. "Prediction of optimal flow front velocity to minimize void formation in dual scale fibrous reinforcements." *International Journal of Material Forming* 7, no. 1: 93-116.

Leclerc, Jean Sébastien and Edu Ruiz. 2008. "Porosity reduction using optimized flow velocity in Resin Transfer Molding." *Composites Part A: Applied Science and Manufacturing* 39, no. 12: 1859-1868.

Little, John Eric, Xiaowen Yuan, and Mark Ian Jones. 2012. "Characterisation of voids in fibre reinforced composite materials." *NDT & E International* 46: 122-127.

Liu, Hai Long, et al. 2014. "Visualization of resin impregnation through opaque reinforcement textiles during the vacuum-assisted resin transfer molding process using ultrasound." *Journal of Composite Materials* 48, no. 9: 1113-1120.

Liu, Ling, et al. 2006. "Effects of cure cycles on void content and mechanical properties of composite laminates." *Composite Structures* 73, no. 3: 303-309.

Liu, Yujie, et al. 2016. *Towards void formation and permeability predictions in LCM processes: A computational bifluid–solid mechanics framework dealing with capillarity and wetting issues*. Vol. 344. http://www.sciencedirect.com.erl.lib.byu.edu/science/article/pii/S1631072116000243.

Loendersloot, Richard. 2006. "The structure-permeability relation of textile reinforcements.".

Lundstrom, T. S. 2000. *The permeability of non-crimp stitched fabrics*. Vol. 31. http://www.sciencedirect.com/science/article/pii/S1359835X00000373.

Lundstrom, T. S., B. R. Gebart, and C. Y. Lundemo. 1993. "Void Formation in RTM." *Journal of Reinforced Plastics and Composites* 12, no. 12: 1339-1349, https://doi.org/10.1177/073168449301201207.

Lundstrom, T. Staffan. 1997. "Measurement of void collapse during resin transfer moulding." *Composites Part A: Applied Science and Manufacturing* 28, no. 3: 201-214.

Lundstrom, T. Staffan and B. Rikard Gebart. 1994. "Influence from process parameters on void formation in resin transfer molding." *Polymer Composites* 15, no. 1: 25-33.

Lystrup, Caleb. 2018. "Permeability Characterization and Fluorescent Void Flow Monitoring for Processing Simulation." *All Theses and Dissertations.* Forthcoming electronic publication to be available at https://scholarsarchive.byu.edu/etd/.

Matsuzaki, Ryosuke, et al. 2014. "Void formation in geometry–anisotropic woven fabrics in resin transfer molding." *Advanced Composite Materials* 23, no. 2: 99-114.

Matuzaki, Ryosuke, et al. 2015. "Analytical prediction of void formation in geometrically anisotropic woven fabrics during resin transfer molding." *Composites Science and Technology*107: 154-161.

Olivier, PBAUPS, J. P. Cottu, and BBAUPS Ferret. 1995. "Effects of cure cycle pressure and voids on some mechanical properties of carbon/epoxy laminates." *Composites* 26, no. 7: 509-515.

Otsu, N. 1979. "A Threshold Selection Method from Gray-Level Histograms." *IEEE transactions on systems, man, and cybernetics* 9, no. 1: 62-66.

Park, Chung Hae, et al. 2011. "Modeling and simulation of voids and saturation in liquid composite molding processes". Vol. 42. http://www.sciencedirect.com/science/article/pii/S1359835X11000492.

Park, Chung Hae and Woo, Lee. 2011. "Modeling void formation and unsaturated flow in liquid composite molding processes: a survey and review." *Journal of Reinforced Plastics and Composites* 30, no. 11: 957-977, https://doi.org/10.1177/0731684411411338.

Patel, N. and L. Lee. 1995. "Effects of fiber mat architecture on void formation and removal in liquid composite molding." *Polymer Composites* 16.

Patel, N. and L. J. Lee. 1996. "Modeling of void formation and removal in liquid composite molding. Part II: Model development and implementation." *Polymer Composites* 17, no. 1: 104-114, https://onlinelibrary.wiley.com/doi/epdf/10.1002/pc.10595.

Patel, N., V. Rohatgi, and L. J. Lee. 1995. "Micro scale flow behavior and void formation mechanism during impregnation through a unidirectional stitched fiberglass mat." *Polymer Engineering and Science* 35: 837+, http://link.galegroup.com/apps/doc/A17183332/AONE?u=byuprovo&sid=AONE&xid=216c6f82.

Ravey, C., E. Ruiz, and F. Trochu. 2014. "Determination of the optimal impregnation velocity in Resin Transfer Molding by capillary rise experiments and infrared thermography."*Composites Science and Technology* 99: 96-102.

Ray, B. C., S. T. Hasan, and D. W. Clegg. 2007. "Evaluation of Defects in FRP Composites by NDT Techniques." *Jnl of Reinforced Plast and Composites* 26, no. 12: 1187-1192.

Richardson, M. O. W. and Z. Y. Zhang. 2000. "Experimental investigation and flow visualisation of the resin transfer mould filling process for non-woven hemp reinforced

phenolic composites." Vol. 31. http://www.sciencedirect.com.erl.lib.byu.edu/science/article/pii/S1359835X00000087.

Rohatgi, V., N. Patel, and L. J. Lee. 1996. "Experimental investigation of flow-induced microvoids during impregnation of unidirectional stitched fiberglass mat." *Polymer Composites* 17, no. 2: 161-170, https://onlinelibrary.wiley.com/doi/epdf/10.1002/pc.10601.

Ruiz, E., et al. 2006. "Optimization of injection flow rate to minimize micro/macro-voids formation in resin transfer molded composites." *Composites Science and Technology* 66, no. 3–4: 475-486.

Saraswat, M. K., D. Heider, and Y. S. Song. 2007. "A qualitative study of the void formation using ultrasounds during the VARTM process.".

Seto, Daigo, et al. 2011. "Void formation in an anisotropic woven fiber during resin transfer molding.".

Shih, Chih-Hsin and L. James Lee. 2002. "Analysis of void removal in liquid composite molding using microflow models." *Polymer composites* 23, no. 1: 120-131.

Sisodia, Sanjay M., et al. 2016. "High-resolution computed tomography in resin infused woven carbon fibre composites with voids." *Composites Science and Technology* 131: 12-21.

Sisodia, Sanjay, et al. 2015. "Effects of voids on quasi-static and tension fatigue behaviour of carbon-fibre composite laminates." *Journal of Composite Materials* 49, no. 17: 2137-2148, https://doi.org/10.1177/0021998314541993.

Stevens, Kimberly. 2018. *Personal Email Communication with Kimberly Stevens*. Received March 23, 2018 by Perry Burton.

Stone, D. E. W. and B. Clarke. 1975. *Ultrasonic attenuation as a measure of void content in carbon-fibre reinforced plastics*. Vol. 8. http://www.sciencedirect.com/science/article/pii/0029102175900237.

Summerscales, John. 2017. "Fibre Distribution and the Process-Property Dilemma." In *The Structural Integrity of Carbon Fiber Composites: Fifty Years of Progress and Achievement of the Science, Development, and Applications*, edited by Peter W. R. Beaumont, Constantinos Soutis, and Alma Hodzic, 301-317. Cham: Springer International Publishing. https://doi.org/10.1007/978-3-319-46120-5_11.

Tang, Jian-Mao, Woo I. Lee, and George S. Springer. 1987. "Effects of cure pressure on resin flow, voids, and mechanical properties." *Journal of Composite Materials* 21, no. 5: 421-440.

Trochu, François, et al. 2006. "Advanced numerical simulation of liquid composite molding for process analysis and optimization." *Composites Part A: Applied Science and Manufacturing* 37, no. 6: 890-902.

Varna, Janis, et al. 1995. "Effect of voids on failure mechanisms in RTM laminates." *Composites Science and Technology* 53, no. 2: 241-249.

Vila, Joaquim, et al. 2015. "An in situ investigation of microscopic infusion and void transport during vacuum-assisted infiltration by means of X-ray computed tomography." *Composites Science and Technology* 119: 12-19.

Villiere, Maxime, et al. 2015. "Dynamic saturation curve measurement in liquid composite molding by heat transfer analysis." *Composites Part A: Applied Science and Manufacturing* 69: 255-265.

Wisnom, Michael R., Tom Reynolds, and Nigel Gwilliam. 1996. "Reduction in interlaminar shear strength by discrete and distributed voids." Composites Science and Technology 56, no. 1: 93-101.

Zobell, Brock Don. 2017. "*In Situ* Characterization of Voids During Liquid Composite Molding." *All Theses and Dissertations*. 6557. https://scholarsarchive.byu.edu/etd/6557

Zobell, Brock and Andrew George. 2017. *In Situ Bubble Characterization During Resin Infusion for Process Simulation of Voids*. Proceedings from 21st International Conference on Composite Materials.